Supporting Information

For

Modulation of Magnetic Behavior via Ligand-Field Effects in the Trigonal Clusters

$(^{Ph}L)Fe_3L^*_3$ (L^* = thf, py, PMe_2Ph)

Emily V. Eames, T. David Harris and Theodore A. Betley*

Department of Chemistry and Chemical Biology, Harvard University
12 Oxford Street, Cambridge MA 02138

Page

Experimental Section S3-S9
Figure S1. UV-vis spectra of **1**, **2**, and **3** S10
Table S1. X-ray Crystallographic Data for **1**, **2**, and **3** S11
Table S2. X-ray Crystallographic Data for **2** from 100-300 K S12
Table S3. Selected Core Bond Distances (Å) for **2** from 100-300 K S13
Table S4. Selected Ligand Bond Distances (Å) at for **1** at 193 K S14
Table S5. Selected Ligand Bond Distances (Å) at for **2** at 100 K S15
Table S6. Selected Ligand Bond Distances (Å) at for **3** at 100 K S16
Figure S2. Solid state molecular structure of **1** S17
Figure S3. Solid state molecular structure of **2** 100 K (A) S18
Figure S4. Solid state molecular structure of **2** 100 K (B) S19
Figure S5. Solid state molecular structure of **2** 150 K S20
Figure S6. Solid state molecular structure of **2** 200 K S21
Figure S7. Solid state molecular structure of **2** 250 K S22
Figure S8. Solid state molecular structure of **2** 300 K S23
Figure S9. Solid state molecular structure of **3** S24
Figure S10. Overlay of the structures of **1**, **2**, and **3** S25
Table S7. ^{57}Fe Mössbauer Fitting Parameters S26
Figure S11. Zero-field ^{57}Fe Mössbauer spectra of **1** at 105 K S27
Figure S12. Zero-field ^{57}Fe Mössbauer spectra of **2** at 4 K S28
Figure S13. Zero-field ^{57}Fe Mössbauer spectra of **2** at 50 K S29
Figure S14. Zero-field ^{57}Fe Mössbauer spectra of **2** at 105 K S30
Figure S15. Zero-field ^{57}Fe Mössbauer spectra of **2** at 150 K S31
Figure S16. Zero-field ^{57}Fe Mössbauer spectra of **2** at 180 K S32
Figure S17. Zero-field ^{57}Fe Mössbauer spectra of **3** at 80 K S33
Figure S18. Zero-field ^{57}Fe Mössbauer spectra of **3** at 110 K S34
Figure S19. Zero-field ^{57}Fe Mössbauer spectra of **3** at 150 K S35
Figure S20. Zero-field ^{57}Fe Mössbauer spectra of **3** at 200 K S36
Figure S21. Zero-field ^{57}Fe Mössbauer spectra of **3** at 250 K S37
Figure S22. $\chi_M T$ versus T (K) for **1** at various applied fields S38

Figure S23. χ^{-1} versus T (K) for **1** at various applied fields S39
Figure S24. Reduced magnetization data for **1** fit with $S = 5$ S40
Figure S25. $\chi_M T$ versus T (K) for **2** at various applied fields S41
Figure S26. χ^{-1} versus T (K) for **2** at various applied fields S42
Figure S27. $\chi_M T$ versus T (K) for **2** with simulations (equilateral) S43
Figure S28. $\chi_M T$ versus T (K) for **2** with simulations (isosceles) S44
Figure S29. $\chi_M T$ versus T (K) for **2** with simulations (scalene) S45
Figure S30. Reduced magnetization data for **2** S46
Figure S31. $\chi_M T$ versus T (K) for **3** at various applied fields S47
Figure S32. χ^{-1} versus T (K) for **3** at various applied fields S48
Figure S33. $\chi_M T$ versus T (K) for **3** with simulations (equilateral) S49
Figure S34. $\chi_M T$ versus T (K) for **3** with simulations (isosceles) S50
Figure S35. $\chi_M T$ versus T (K) for **3** with simulations (scalene) S51
Figure S36. Reduced magnetization data for **3** S52

Experimental Section

Materials and Methods. All manipulations involving metal complexes were carried out using standard Schlenk line or glove-box techniques under a dinitrogen atmosphere. All glassware was oven-dried for a minimum of 4 h and cooled in an evacuated antechamber prior to use in the dry box. Benzene, toluene, diethyl ether, hexanes and tetrahydrofuran (THF) were dried and deoxygenated on a Glass Contour System (SG Water USA, Nashua, NH) and stored over 4 Å molecular sieves (Strem) prior to use. Dimethylsulfoxide-d_6 and chloroform-d were purchased from Cambridge Isotope Labs and used as received. Benzene-d_6 and THF-d_8 were purchased from Cambridge Isotope Labs and were degassed and stored over 4 Å molecular sieves prior to use. Non-halogenated solvents were typically tested with a standard purple solution of sodium benzophenone ketyl in THF in order to confirm effective oxygen and moisture removal. $MeC(CH_2NHPh\text{-}o\text{-}NH_2)_3$ (^{H}L)[1], $Fe_2(N(Si(CH_3)_2)_2)_4$[2] and Fe_2Mes_4 (Mes = 2,4,6-$Me_3C_6H_2$)[3] were prepared following published methods. Anhydrous pyridine was purchased from Aldrich and stored over 4 Å molecular sieves prior to use. $Pd_2(dba)_3$ (Strem), bromobenzene (Aldrich), sodium tert-butoxide (Aldrich), BINAP (Strem), PMe_2Ph (Strem) were used as received. All other reagents were purchased from commercial vendors and used without further purification unless explicitly stated.

Physical Measurements. All of the measurements for the metal complexes were made under anaerobic conditions. Elemental analyses were performed by Complete Analysis Laboratories, Inc., Parsippany, New Jersey or Robertson Microlit Laboratories, Madison, New Jersey. ^{1}H and ^{13}C NMR spectra were recorded on a Varian Unity/Inova 500B or Varian Mercury 400B NMR spectrometer with chemical shifts (δ ppm) referenced to residual NMR solvent. UV/Visible spectra were recorded on a Varian Cary 50 UV/Visible spectrometer using quartz cuvettes. NIR spectra were recorded on a PerkinElmer Lambda 750 high-performance UV-vis spectrometer. The spectrum of **3** was recorded in benzene with excess PMe_2Ph to maintain the stability of the complex and blanked appropriately with the solution used for dilution of the sample. The spectra of **1** and **2** were recorded in THF and benzene respectively for the same reason; if **2** is collected in THF the spectrum resembles that of **1**.

Magnetic measurements were recorded using a Quantum Design MPMS-5S magnetometer. Samples were suspended in the magnetometer in folded plastic bags or suspended in eicosane wax contained in Lilly #4 gel capsules, inserted into plastic straws. All manipulations were performed under an atmosphere of dinitrogen. Dc magnetic susceptibility data were collected in the temperature range 2-300 K under fields of 0.1, 0.5, 1 and 2 T. Magnetization data were acquired at 1.8-10 K under fields of 1, 2, 3, 4, 5, 6, and 7 T. Susceptibility data were corrected for the diamagnetic contribution of a blank sample consisting of the bag or wax, capsule and straw at the correct field and temperature. The magnetic susceptibilities were adjusted for diamagnetic contributions using the constitutive corrections from Pascal's constants. The molar magnetic susceptibility (χ_m) was calculated by converting the magnetization (M) obtained from the magnetometer to a molar susceptibility using the multiplication factor [molecular weight (MW)]/[sample weight (m) × field strength (H)].

Iron-57 Mössbauer spectra were measured on a constant acceleration spectrometer (SEE Co, Minneapolis, MN) with a Janis SVT-100 cryostat. Isomer shifts are quoted relative to α-Fe foil (< 25 μm thick) at room temperature. The Fe foil standard spectrum has linewidths Γ (FWHM) of 0.292 and 0.326 mm/s for the doublets within the ±4 mm/s window when measured outside the cryostat at room temperature. Samples were prepared using approximately 30 mg of sample suspended in paratone-N oil (**1** and **2**) or eicosane wax (**3**). Data for **2** and **3** were collected at multiple temperatures. Temperatures were controlled using a LakeShore 321 Autotuning temperature controller. Temperature swings were no greater than ±10 K, and were generally within ±2 K.

Data were analyzed using an in-house package written by E. R. King and modified by E. V. Eames in Igor Pro (Wavemetrics). Initially a simple model consisting of Lorentzian lineshapes with optional asymmetry was used. However, both compounds **2** and **3** show temperature-dependent asymmetry in the doublet peaks, which suggests that a relaxation process between two states with differing hyperfine parameters may be present. Accordingly, the data were fit with a relaxation model following the approach of Litterst and Amthauer.[4] This model supposes that two states of differing hyperfine parameters exist for a given Fe atom, with transition probability per second λ. The fitting expression used was

$$\phi(\omega) \propto \frac{(\Gamma/2+\lambda)A-(\omega-p_1\varepsilon_2-p_2\varepsilon_1)B}{A^2+B^2}+\frac{(\Gamma/2+\lambda)A'-(\omega-p_1\varepsilon'_2-p_2\varepsilon'_1)B'}{A'^2+B'^2}$$

with

$$\begin{aligned}
A &= (\omega-\varepsilon_1)(\omega-\varepsilon_2)-\Gamma/2(\Gamma/2+\lambda)\\
A' &= (\omega-\varepsilon'_1)(\omega-\varepsilon'_2)-\Gamma/2(\Gamma/2+\lambda)\\
B &= (\Gamma+\lambda)\omega-\Gamma/2(\varepsilon_1+\varepsilon_2)-\lambda(p_1\varepsilon_1+p_2\varepsilon_2)\\
B' &= (\Gamma+\lambda)\omega-\Gamma/2(\varepsilon'_1+\varepsilon'_2)-\lambda(p_1\varepsilon'_1+p_2\varepsilon'_2)\\
\varepsilon_1 &= S_1+\Delta_1/2\\
\varepsilon'_1 &= S_1-\Delta_1/2\\
\varepsilon_2 &= S_2+\Delta_2/2\\
\varepsilon'_2 &= S_2-\Delta_2/2
\end{aligned}$$

where Γ is the full width at half maximum (FWHM), and S_n is the chemical shift, Δ_n is the quadrupole splitting, and p_n is the population of state n. For comparison in all fits with both models, the linewidth Γ was held constant at 0.32 mm/s, which is the best fit FWHM observed for both compounds at the lowest temperature. In both cases, the overlap between the doublets resulted in fits of similar quality with a variety of parameter values, precluding a conclusive interpretation. Fits were attempted using both the same sign of electric field gradient for both components and opposite signs, but there was little difference between the two; fits with the same sign are shown. Compound 2 can be fit using the relaxation model to yield a plausible set of parameters, with the relaxation rate λ and the population of the major doublet increasing with temperature, and the isomer shifts and quadrupole splittings decreasing. However, the fits do not model the asymmetry of the peaks very well. Compound 3 cannot be modelled convincingly with this method, as at most temperatures fits yield a relaxation rate of zero, implying that a simple model consisting of four Lorentzians is preferred.

Preparation of $MeC(CH_2NHPh$-*o*-$NHPh)_3$ ($^{Ph}LH_6$): $Pd_2(dba)_3$ (103 mg, 112 µmol, 2.2 mol %) and BINAP (211 mg, 337 µmol, 6.6 mol %) were dissolved in 15 mL toluene and heated to 35 ºC for 40 min, then filtered and combined with $MeC(CH_2NHPh$-*o*-$NH_2)_3$ (2 g, 5.12 mmol, 1 equiv), bromobenzene (2.42 g, 15.4 mmol, 3 equiv), sodium tert-butoxide (1.97 g, 20.5 mmol, 4 equiv) and toluene (200 mL) and heated in a sealed bomb at 70 ºC for 18 h. The product was extracted with dichloromethane, washed twice with water, dried over Na_2SO_4, filtered and the solvent removed under reduced pressure. The resulting pale yellow solid was washed with ether and dried under vacuum to yield 2.54 g, (80%). ^{1}H NMR ($CDCl_3$, 500 MHz, δ, ppm): 7.12 (t, 6H, aromatic C-*H*, *J* = 7.6 Hz), 7.06-7.04 (m, 6H, aromatic C-*H*), 6.78 (t, 3H, aromatic C-*H*, *J* = 7.5 Hz), 6.69 (d, 3H, aromatic C-*H*, *J* = 7.5 Hz), 6.58 (d, 3H, aromatic C-*H*, *J* = 8.0 Hz), 6.56 (d, 6H, aromatic C-*H*, *J* = 7.0 Hz), 3.04 (s, 6H, -NH-CH_2-C), 0.86 (s, 3H, -C-CH_3); ^{13}C NMR (C_6D_6, 500 MHz, δ, ppm): 146.21, 145.01, 129.36, 126.91, 126.41, 121.48, 119.25, 117.47, 115.06, 111.43, 49.80, 39.17, 20.53; HRMS (ESI$^+$) *m/z* calcd $C_{41}H_{37}N_6^+$ $[M+H]^+$: 619.35437, found 619.35488.

Preparation of (^{Ph}L)$Fe_3(THF)_3$ (1). To a frozen solution of $^{Ph}LH_6$ (1 g, 1.6 mmol, 1 equiv) in THF (15 ml) and diethyl ether (200 mL) was added $Fe_2(N(Si(CH_3)_2)_2)_4$ (1.83 g, 4.87 mmol, 3 equiv) as a solution in diethyl ether (20 mL). The solution was allowed to thaw with stirring. After stirring for 3 h, the brown solution was concentrated to 40 mL and stored at –35 °C for 24 h. The resulting brown crystals were washed with THF. Analytical samples were recrystallized under similar conditions. Yield: 0.99 g (60%) after first crystallization; additional product could be isolated by concentrating solution and washes for a second batch of crystals. ^{1}H NMR (C_6D_6, 500 MHz, δ, ppm): 37, 17, 10, 6, -5, -46, -53, -70. UV-vis (THF) (λ_{max}/nm ((ε/$M^{-1}cm^{-1}$)) 428 (5800), 590 (2000, sh), 760, (1700). Anal. Calcd for $C_{53}H_{60}Fe_3N_6O_3$: C 63.87, H 6.07, N 8.43. Found: C 63.82, H 5.95, N 8.24.

Preparation of (^{Ph}L)$Fe_3(py)_3$ (2). To a frozen solution of Fe_2Mes_4 (2.86 g, 4.8 mmol, 1.5 equiv) in THF (100 mL) was added pyridine (842 mg, 9.6 mmol, 3 equiv). The solution was allowed to thaw with stirring, then frozen and $^{Ph}LH_6$ (2 g, 3.2 mmol, 1 equiv) in 25 ml cold THF was added. The reaction was stirred for 18 h, then concentrated and filtered with THF or ether. The product was precipitated at –35 °C in the presence of excess pyridine as a brown powder, washed with hexanes, and dried under vacuum overnight. Yield: 2.18 g (66%). X-ray quality crystals were grown from a concentrated solution in benzene with a drop of pyridine at room temperature. ^{1}H NMR (C_6D_6, 500 MHz, δ, ppm): 88, 32, 25, 14, 12, 9, -31, -36, -39. UV-vis (benzene) (λ_{max}/nm ((ε/M^{-1}cm^{-1}) 490 (6100, sh). IR (KBr pellet) 1592, 1474, 1443, 746, 695 cm^{-1}. Anal. Calcd for $C_{56}H_{52}Fe_3N_9$: C 66.10, H 5.05, N 12.39. Found: C 66.04, H 5.38, N 12.36.

Preparation of (^{Ph}L)$Fe_3(PMe_2Ph)_3$ (3). (^{Ph}L)$Fe_3(THF)_3$ (230 mg, 231 nmol) was dissolved in THF and diethyl ether (1:1, 15 mL) and chilled. PMe_2Ph was added (160 mg, 5 equiv) in 2 mL diethyl ether and the brown mixture was stirred at RT for 4 h. The solution was chilled at –35 °C following the addition of 5 ml hexanes. Some crystalline product was obtained and washed with hexanes (72 mg) and additional product was precipitated by addition of the solution to 30 ml hexanes at freeze temperature (106 mg) for a total yield of 65%. X-ray quality crystals were grown from a concentrated solution of benzene at RT. Analytical samples were precipitated from concentrated THF/diether ether solution with excess phosphine at –35 °C. ^{1}H NMR (C_6D_6, 500 MHz, δ, ppm): 29, 17, 13, 11, 9, 0, -2, -9, -17, -18, -20. UV-vis (benzene) (λ_{max}/nm ((ε/M^{-1}cm^{-1}) 490 (6600, sh) 730 (2300, sh). Anal. Calcd for $C_{65}H_{69}Fe_3N_6P_3$: C 65.35, H 5.82, N 7.03. Found: C 65.27, H 5.81, N 6.92.

X-ray Structure Determinations. A single crystal suitable for X-ray analysis was mounted and centered on the tip of a cryoloop attached to a goniometer head. Data for **2** were collected at 100 K, 150 K, 200 K, 250 K and 300 K on an APEX II CCD single crystal diffractometer on a single crystal, warming at a rate of 120 K/h between collections. Cell parameters were determined using the program SMART.[5] Data reduction and integration were performed with the software package SAINT,[6] while absorption corrections were applied using the program SADABS.[7] Space groups were assigned unambiguously by analysis of symmetry, and systematic absences were determined by XPREP. The positions of the heavy atoms were found via direct methods using the program SHELXTL.[8] Subsequent cycles of least-squares refinement followed by difference Fourier syntheses revealed the positions of the remaining non-hydrogen atoms. Hydrogen atoms were added in idealized positions. Non-hydrogen atoms were refined with anisotropic displacement parameters. The space group for **3** was confirmed by Platon. Crystallographic data are given in Tables S1-2 and selected bond distances and angles in Tables S3-7.

---

(1) Zhao, Q.; Betley, T. A. *Angew. Chem. Int. Ed.*, **2011**, *50*, 709.

(2)Andersen, R. A.; Faegri, K.; Green, J. C.; Haaland, A.; Lappert, M. F.; Leung, W.-P.; Rypdal, K., *Inorg. Chem.* **1988,** 27, 1782.

(3) Klose, A.; Solari, E.; Ferguson, R.; Floriani, C.; Chiesi-Villa, A.; Rizzoli, C. *Organometallics* **1993**, *12*, 2414.

(4) Litterst, F. J.; Amthauer, G., *Phys Chem Minerals* **1984**, *10*, 250.

(5) SMART V 5.05 Software for the CCD Detector System; Bruker Analytical X-ray System, Inc.: Madison, WI, 1998.

(6) SAINT. Data Reduction Software. V 6.36A; Bruker Analytical X-ray System, Inc.: Madison, WI, 2002.

(7) SADABS. Bruker/Siemens Area Detector Absorption and Other Corrections. V2.03; Bruker Analytical X-ray System, Inc.: Madison, WI, 2002.

(8) Sheldrick, G. M., *SHELXTL. V 6.12*; Bruker Analytical X-ray Systems, Inc.: Madison, WI, 2000.

Figure S1. UV-vis spectra of **1** in THF (green), **2** in benzene (red) and **3** in benzene (blue).

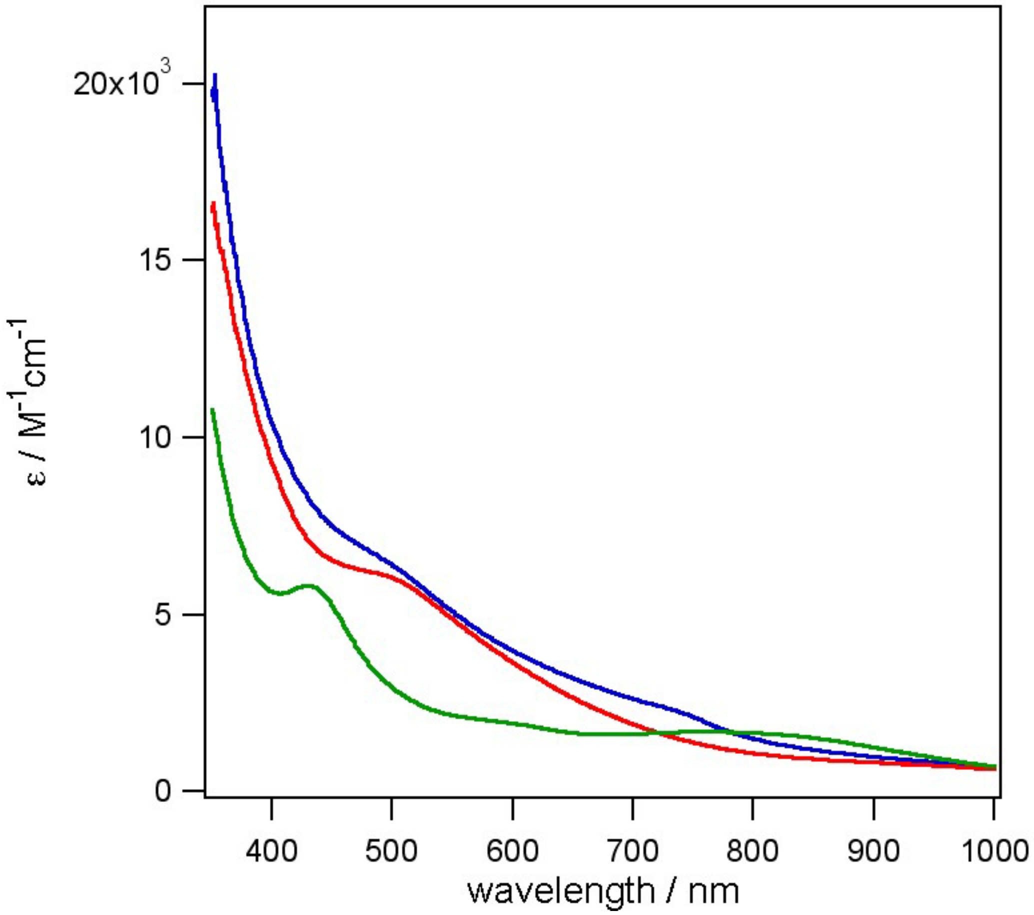

Table S1. X-ray Crystallographic Data for **1**, **2** and **3**.

Chemical formula	$C_{53}H_{60}Fe_3N_6O_3$ $\cdot 1.75(C_4H_8O)$	$C_{56}H_{51}Fe_3N_9$ $\cdot 2(C_6H_6)$	$C_{65}H_{69}Fe_3N_6P_3$
FW	1122.80	1173.82	1194.73
Space group	*C2/c*	$P\bar{1}$	*P2(1)/c*
a (Å)	21.1077(18)	11.805(2)	12.403(3)
b (Å)	15.5695(13)	12.980(2)	20.060(4)
c (Å)	33.842(3)	19.363(4)	22.036(5)
α (deg)	90	73.794(3)	90
β (deg)	98.773(6)	86.132(3)	90
γ (deg)	90	75.907(3)	90
V (Å^3)	10991.5(16)	2763.4(9)	5483(2)
Z	8	2	4
d_{calcd} (g·cm^{-3})	1.357	1.411	1.447
μ (mm^{-1})	0.835	0.83	0.920
T (K)	193(2)	100(2)	100(2)
R1^a (wR2^b)	0.0635 (0.1819)	0.0733 (0.1461)	0.0625 (0.1096)

[a] $R1 = [\sum w(F_o - F_c)^2 / \sum w F_o^2]^{1/2}$.

[b] $wR2 = [\sum [w(F_o^2 - F_c^2)^2] / \sum w(F_o^2)^2]^{1/2}$, $w = 1/[\sigma^2(F_o^2) + (aP)^2 + bP]$, where $P = [\max(F_o^2,0) + 2(F_c^2)]/3$.

Table S2. X-ray Crystallographic Data of **2** from 100-300 K.

Chemical formula	$C_{56}H_{51}Fe_3N_9 \cdot 2(C_6H_6)$	$C_{56}H_{51}Fe_3N_9 \cdot 2(C_6H_6)$	$C_{56}H_{51}Fe_3N_9 \cdot 2(C_6H_6)$	$C_{56}H_{51}Fe_3N_9 \cdot 2(C_6H_6)$	$C_{56}H_{51}Fe_3N_9 \cdot 2(C_6H_6)$	$C_{56}H_{51}Fe_3N_9 \cdot 2(C_6H_6)$
fw	1173.82	1173.82	1173.82	1173.82	1173.82	1173.82
Space group	$P\bar{1}$	$P\bar{1}$	$P\bar{1}$	$P\bar{1}$	$P\bar{1}$	$P\bar{1}$
a (Å)	11.805(2)	11.839(4)	11.8394(18)	11.888(3)	11.881(3)	11.8228(15)
b (Å)	12.980(2)	13.026(5)	13.037(2)	13.106(3)	13.093(4)	13.0025(16)
c (Å)	19.363(4)	19.436(7)	19.508(3)	19.649(4)	19.706(6)	19.398(3)
α (deg)	73.794(3)	73.818(6)	73.852(3)	73.904(4)	73.971(5)	73.786(2)
β (deg)	86.132(3)	86.197(7)	86.214(3)	86.251(4)	86.265(5)	86.134(3)
γ (deg)	75.907(3)	75.893(7)	75.811(3)	75.708(4)	75.654(5)	75.919(7)
V (Å^3)	2763.4(9)	2791.6(18)	2804.0(7)	2850.5(11)	2854.3(14)	2777.3(6)
Z	2	2	2	2	2	2
d_{calcd} (g·cm^{-3})	1.411	1.396	1.39	1.368	1.366	1.404
μ (mm^{-1})	0.83	0.822	0.818	0.805	0.804	0.826
T (K)	**100(2)**	**150(2)**	**200(2)**	**250(2)**	**300(2)**	**100(2)**
R1[a] (wR2[b])	0.0733 (0.1461)	0.0678 (0.1188)	0.0568 (0.1007)	0.0597 (0.1117)	0.0691 (0.1229)	0.0954 (0.2017)

[a] $\mathrm{R1} = [\sum w(F_o - F_c)^2/\sum wF_o^2]^{1/2}$.

[b] $\mathrm{wR2} = [\sum [w(F_o^2 - F_c^2)^2]/\sum w(F_o^2)^2]^{1/2}$, $w = 1/[\sigma^2(F_o^2) + (aP)^2 + bP]$, where $P = [\max(F_o^2,0) + 2(F_c^2)]/3$.

Table S3. Selected Core Bond Distances (Å) of **2** from 100-300 K.

Temperature (K)	100	150	200	250	300
Fe(1)–Fe(2)	2.6074(6)	2.5981(10)	2.5898(6)	2.5967(7)	2.5917(8)
Fe(1)–Fe(3)	2.5466(6)	2.5327(8)	2.5254(5)	2.5357(6)	2.5370(7)
Fe(2)–Fe(3)	2.5756(6)	2.5658(10)	2.5648(6)	2.5757(7)	2.5765(8)
Fe(1)–N(1L)	2.091(2)	2.108(2)	2.110(2)	2.117(2)	2.116(2)
Fe(2)–N(2L)	2.115(2)	2.124(2)	2.126(2)	2.136(2)	2.133(2)
Fe(3)–N(3L)	2.119(2)	2.125(2)	2.128(2)	2.127(2)	2.123(3)
Fe(1)–N(2)	2.193(2)	2.194(2)	2.1972(19)	2.200(2)	2.188(2)
Fe(1)–N(3)	2.137(2)	2.138(2)	2.1392(19)	2.143(2)	2.132(2)
Fe(1)–N(5)	2.109(2)	2.111(2)	2.1020(19)	2.108(2)	2.102(2)
Fe(1)–N(6)	2.228(2)	2.224(2)	2.2281(19)	2.242(2)	2.248(2)
Fe(2)–N(1)	2.208(2)	2.203(2)	2.202(2)	2.204(2)	2.193(2)
Fe(2)–N(3)	2.1263(19)	2.134(2)	2.1337(18)	2.144(2)	2.140(2)
Fe(2)–N(4)	2.1277(19)	2.131(2)	2.1346(19)	2.146(2)	2.146(2)
Fe(2)–N(6)	2.146(2)	2.149(2)	2.1388(19)	2.141(2)	2.132(2)
Fe(3)–N(1)	2.078(2)	2.081(2)	2.0871(19)	2.090(2)	2.087(2)
Fe(3)–N(2)	2.0928(19)	2.094(2)	2.0899(19)	2.096(2)	2.092(2)
Fe(3)–N(4)	2.269(2)	2.266(2)	2.2578(19)	2.263(2)	2.250(2)
Fe(3)–N(5)	2.221(2)	2.227(2)	2.2287(19)	2.242(2)	2.243(2)

Table S4. Selected Ligand Bond Distances (Å) for **1** at 193 K.

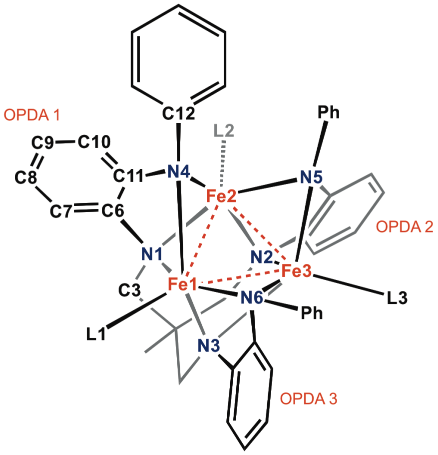

OPDA subunit	**1**	**2**	**3**
C(3)–N(1)	1.456(7)	1.465(7)	1.455(7)
N(1)–C(6)	1.398(7)	1.406(7)	1.401(7)
C(6)–C(7)	1.387(8)	1.388(8)	1.387(8)
C(7)–C(8)	1.396(8)	1.402(7)	1.394(8)
C(8)–C(9)	1.350(8)	1.361(9)	1.371(8)
C(9)–C(10)	1.404(8)	1.384(9)	1.388(8)
C(10)–C(11)	1.381(8)	1.388(8)	1.392(7)
C(6)–C(11)	1.407(7)	1.404(8)	1.422(7)
C(11)–N(4)	1.434(7)	1.417(7)	1.415(7)
N(4)–C(12)	1.425(7)	1.425(7)	1.429(7)

Table S5. Selected Ligand Bond Distances (Å) for **2** at 100 K.

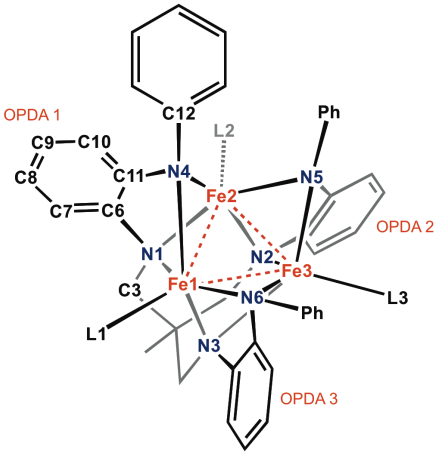

OPDA subunit	**1**	**2**	**3**
C(3)–N(1)	1.452(3)	1.450(3)	1.449(3)
N(1)–C(6)	1.392(3)	1.394(3)	1.394(3)
C(6)–C(7)	1.385(3)	1.384(3)	1.387(3)
C(7)–C(8)	1.396(3)	1.388(3)	1.395(3)
C(8)–C(9)	1.359(3)	1.373(3)	1.369(3)
C(9)–C(10)	1.383(3)	1.389(3)	1.388(3)
C(10)–C(11)	1.389(3)	1.386(3)	1.391(3)
C(6)–C(11)	1.407(3)	1.408(3)	1.404(3)
C(11)–N(4)	1.410(3)	1.409(3)	1.403(3)
N(4)–C(12)	1.420(3)	1.422(3)	1.419(3)

Table S6. Selected Ligand Bond Distances (Å) for **3** at 100 K.

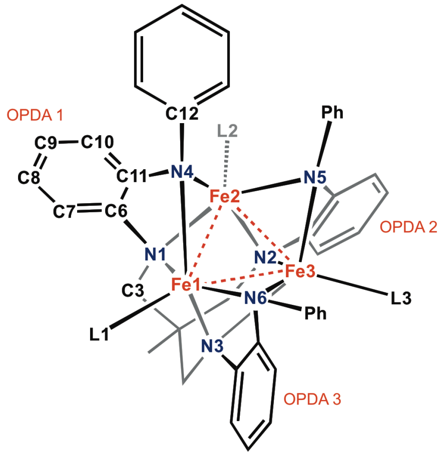

OPDA subunit	**1**	**2**	**3**
C(3)–N(1)	1.455(7)	1.469(7)	1.454(7)
N(1)–C(6)	1.387(7)	1.392(7)	1.394(7)
C(6)–C(7)	1.372(8)	1.369(8)	1.386(8)
C(7)–C(8)	1.382(8)	1.385(8)	1.381(8)
C(8)–C(9)	1.368 (8)	1.373(8)	1.365(8)
C(9)–C(10)	1.377(8)	1.380(8)	1.397(8)
C(10)–C(11)	1.364(8)	1.383(8)	1.380(8)
C(6)–C(11)	1.418(8)	1.420(8)	1.401(8)
C(11)–N(4)	1.414(7)	1.403(7)	1.401(7)
N(4)–C(12)	1.434(7)	1.393(7)	1.416(7)

Figure S2. Solid state structure of **1** at 193 K with the thermal ellipsoids set at the 50% probability level (hydrogen atoms and solvent molecules omitted for clarity; only one site shown for disordered atoms; Fe orange, C black, N blue, O red). Top view (above); side view, THF carbon atoms omitted for clarity (below).

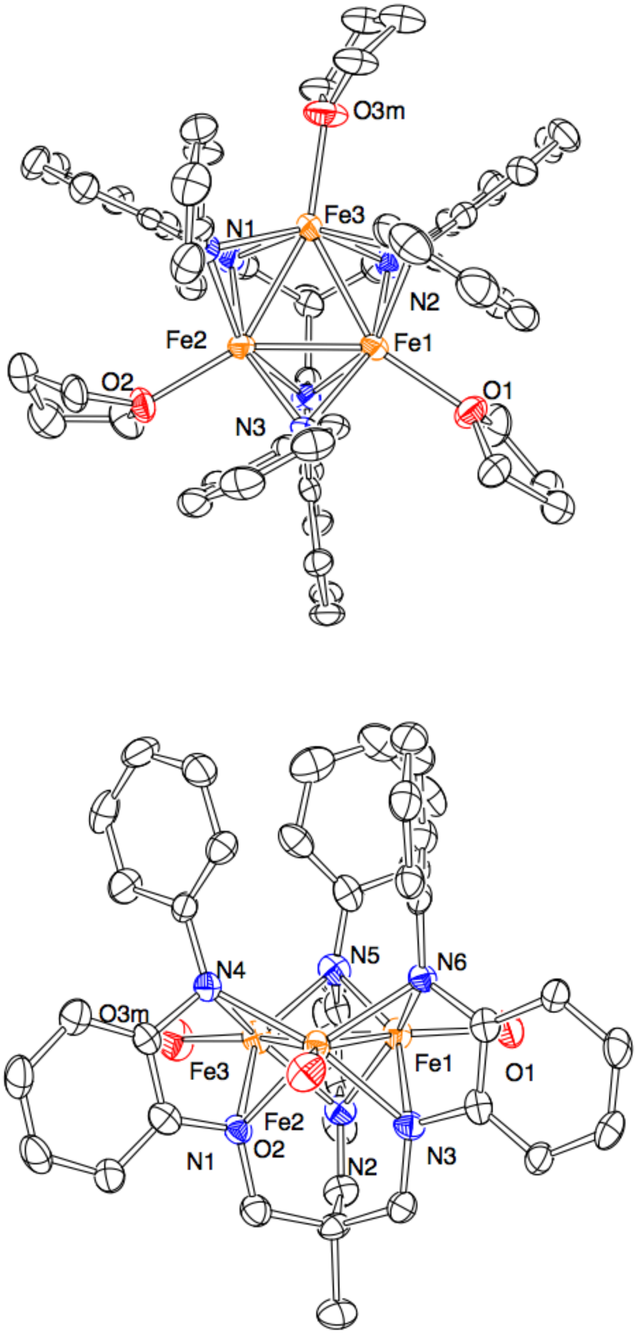

Figure S3. Solid state structure of **2** at 100 K (first collection) with the thermal ellipsoids set at the 50% probability level (hydrogen atoms and solvent molecules omitted for clarity; Fe orange, C black, N blue). Top view (above); side view, pyridine carbon atoms omitted for clarity (below).

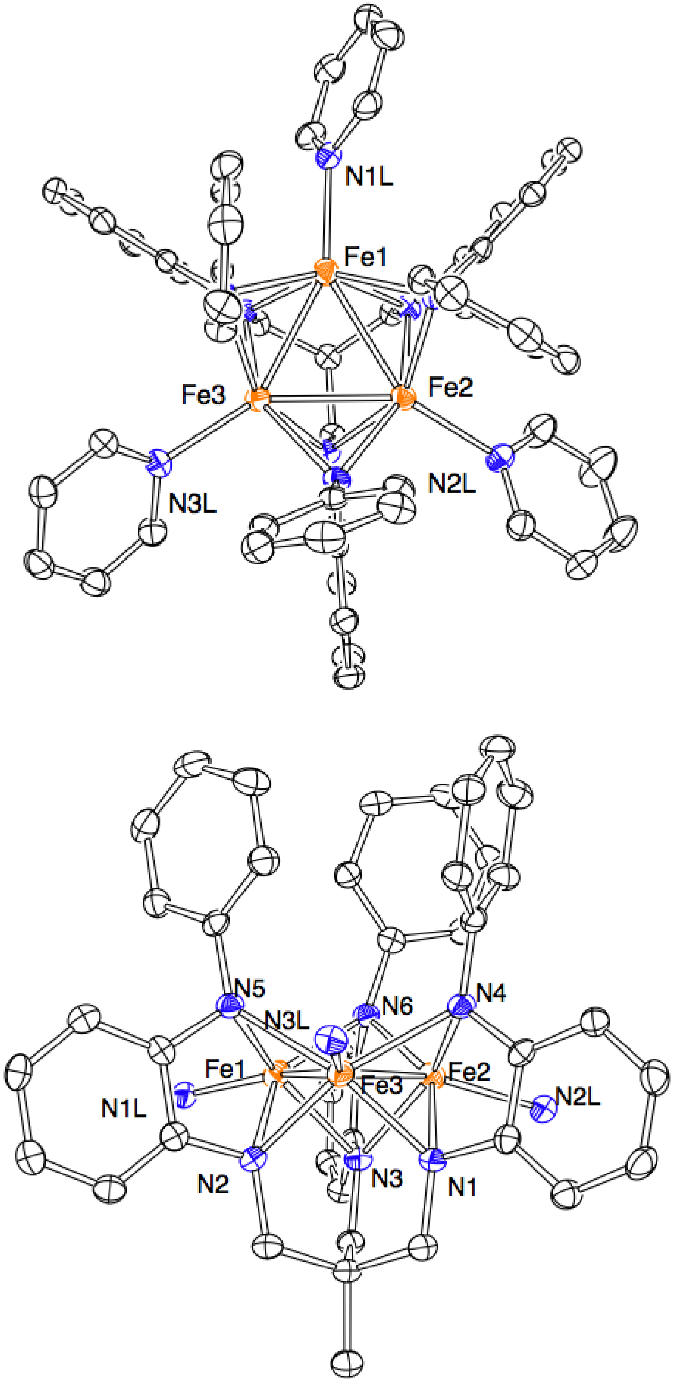

Figure S4. Solid state structure of **2** at 100 K (second collection) with the thermal ellipsoids set at the 50% probability level (hydrogen atoms and solvent molecules omitted for clarity; Fe orange, C black, N blue). Top view (above); side view, pyridine carbon atoms omitted for clarity (below).

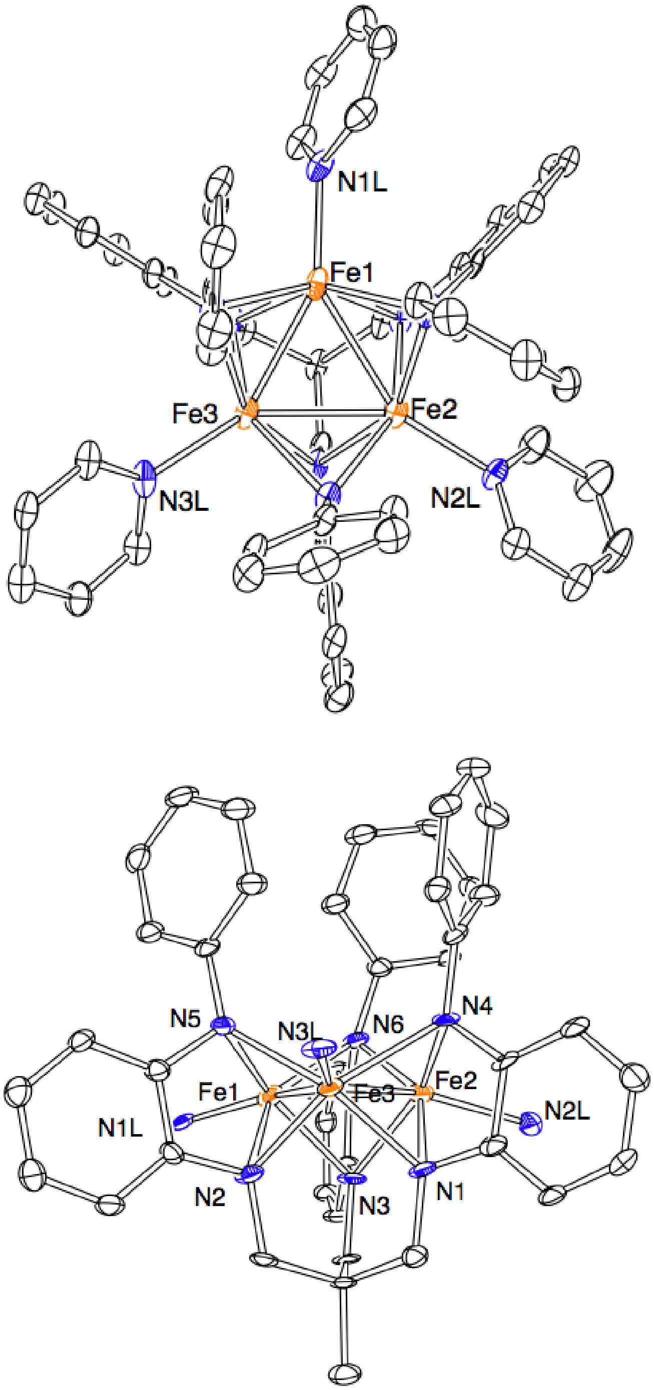

Figure S5. Solid state structure of **2** at 150 K with the thermal ellipsoids set at the 50% probability level (hydrogen atoms and solvent molecules omitted for clarity; Fe orange, C black, N blue). Top view (above); side view, pyridine carbon atoms omitted for clarity (below).

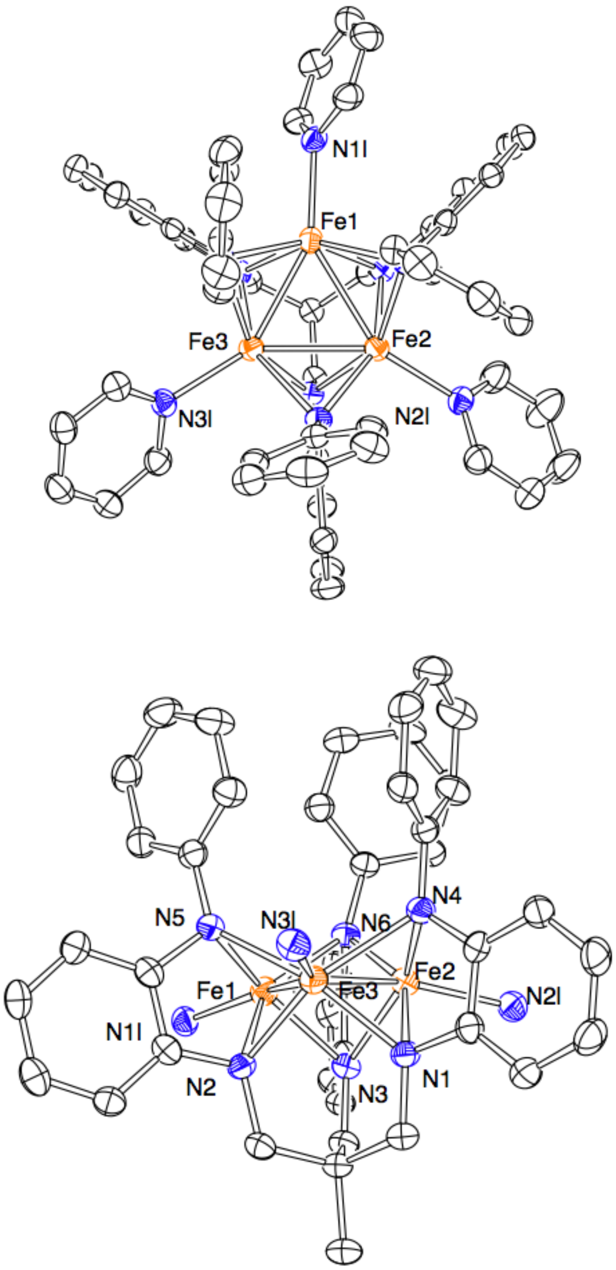

Figure S6. Solid state structure of **2** at 200 K with the thermal ellipsoids set at the 50% probability level (hydrogen atoms and solvent molecules omitted for clarity; Fe orange, C black, N blue). Top view (above); side view, pyridine carbon atoms omitted for clarity (below).

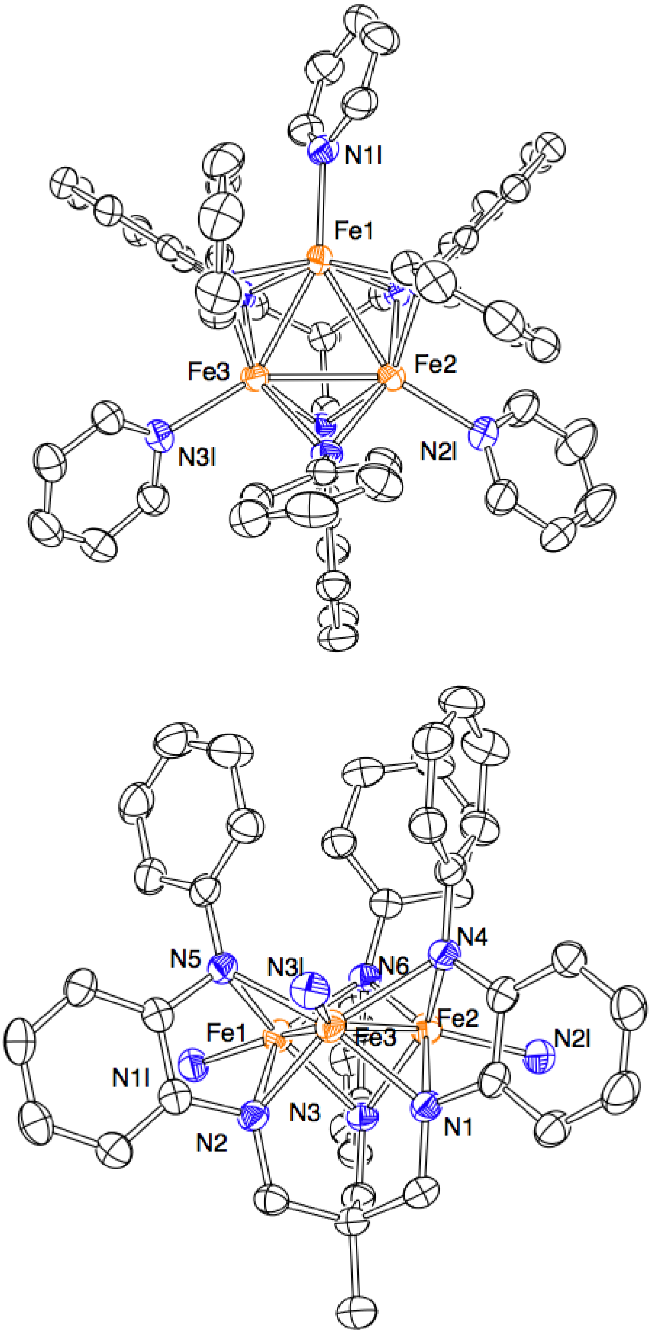

Figure S7. Solid state structure of **2** at 250 K with the thermal ellipsoids set at the 50% probability level (hydrogen atoms and solvent molecules omitted for clarity; Fe orange, C black, N blue). Top view (above); side view, pyridine carbon atoms omitted for clarity (below).

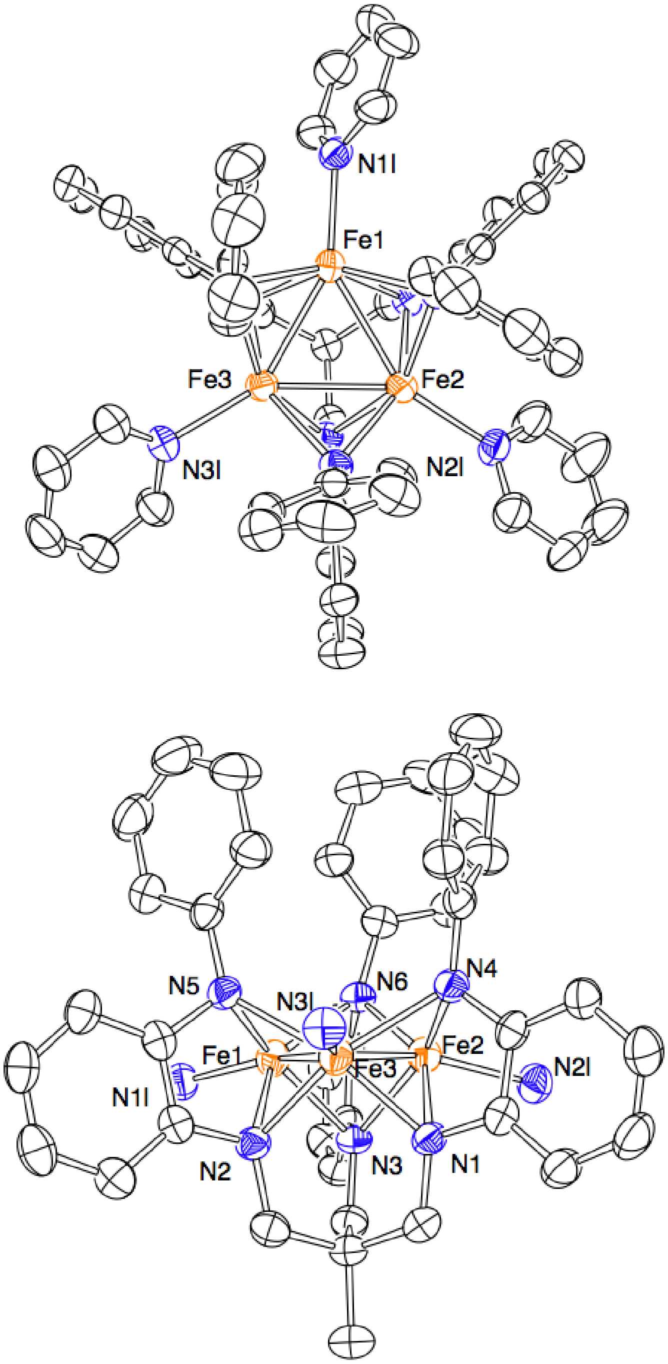

Figure S8. Solid state structure of **2** at 300 K with the thermal ellipsoids set at the 50% probability level (hydrogen atoms and solvent molecules omitted for clarity; Fe orange, C black, N blue). Top view (above); side view, pyridine carbon atoms omitted for clarity (below).

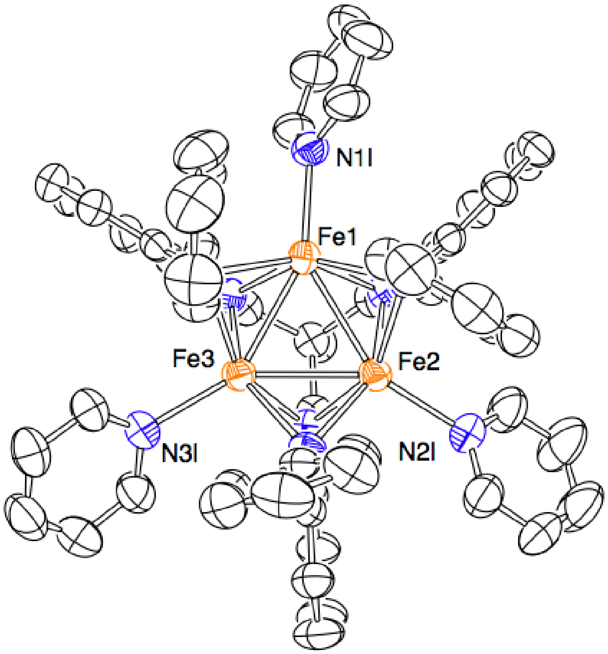

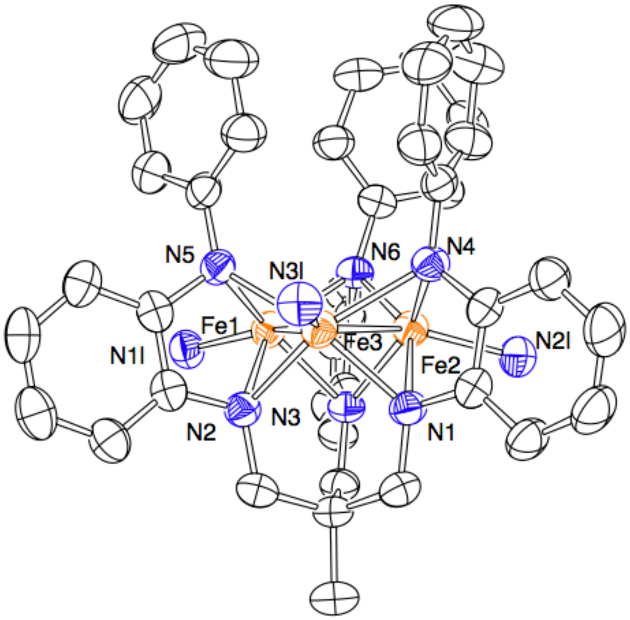

Figure S9. Solid state structure of **3** at 100 K with the thermal ellipsoids set at the 50% probability level (hydrogen atoms omitted for clarity; Fe orange, C black, N blue, P magenta). Top view (above); side view, PMe_2Ph carbon atoms omitted for clarity (below).

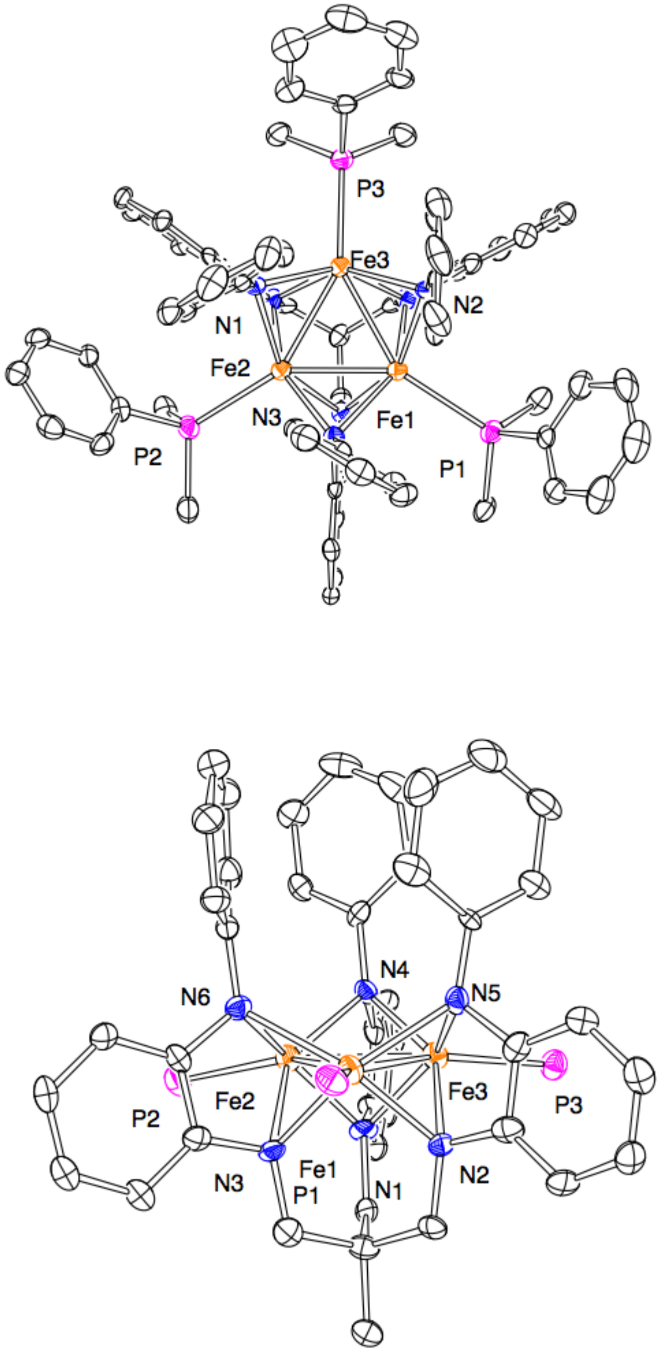

Figure S10. Overlay of the structures of **1** (green), **2** (at 100K, red) and **3** (blue), carbon and hydrogen atoms omitted for clarity. Top view (above); side view (below).

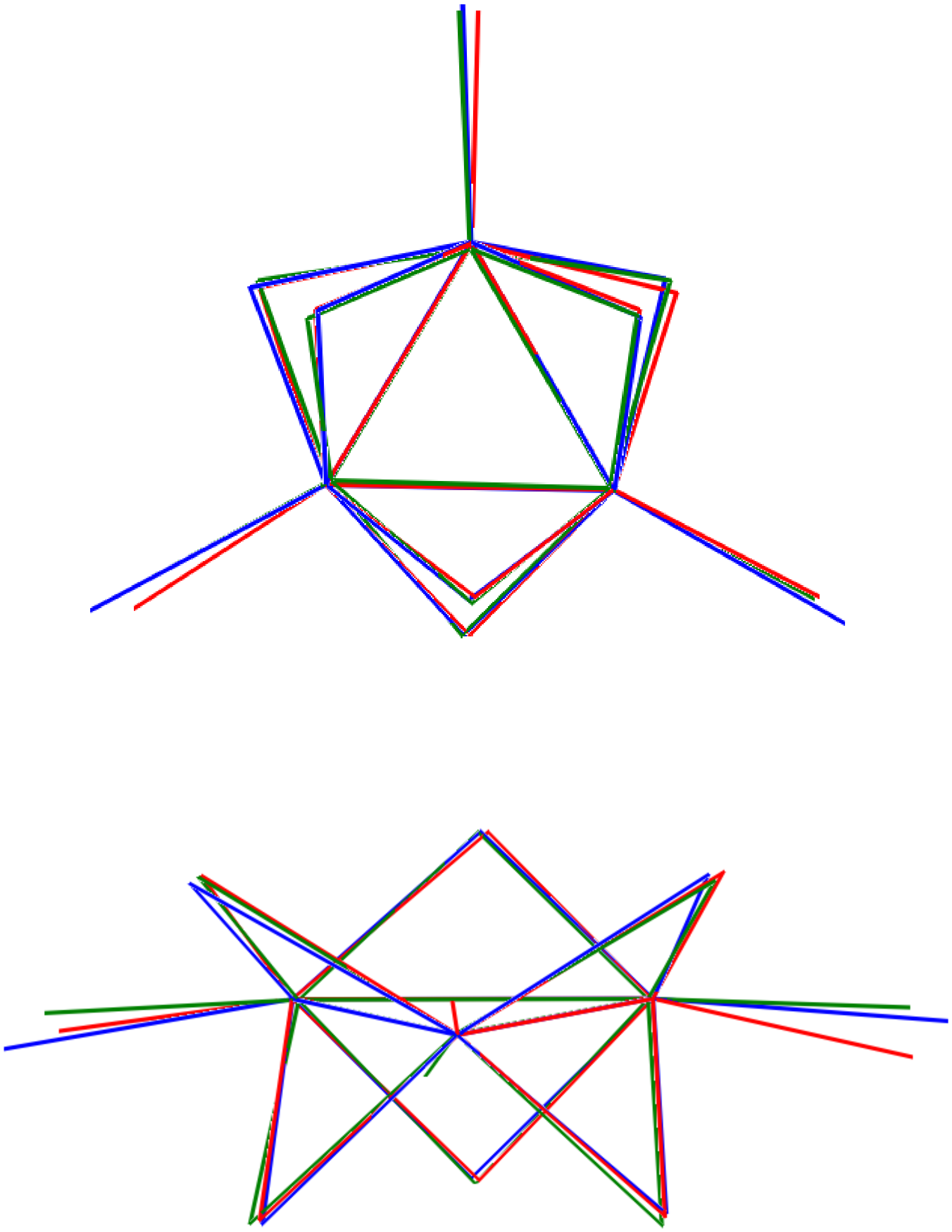

Table S7. ^{57}Fe Mössbauer fitting parameters. Errors in δ, ΔE_Q and FWHM (2γ) are <0.01 mm/s unless otherwise specified.

Compound	T (K)	Fit type	λ (kHz)	δ (mm/s)	ΔE_Q (mm/s)	%	FWHM (mm/s) (left area:right area, if allowed to vary)
1	105	Lorentzian		0.79	1.25	100	0.52 (left, 47%) 0.43 (right, 53%)
2	4	relaxation	35 ± 40	0.83	1.57	64	0.32
				0.87	2.76	36	0.32
		Lorentzian		0.83	1.57	64	0.32 (51:49)
				0.87	2.76	36	0.32 (50:50)
	50	relaxation	750 ± 60	0.83	1.55	64	0.32
				0.88	2.76	36	0.32
		Lorentzian		0.83	1.59	65	0.32 (52:48)
				0.88	2.71	35	0.32 (49:51)
	105	relaxation	1110±50	0.82	1.45	70	0.32
				0.87	2.33	30	0.32
		Lorentzian		0.82	1.48	71	0.32 (51:49)
				0.85	2.22	29	0.32 (50:50)
	150	relaxation	1290±350	0.80	1.37	80	0.32
				0.85±0.02	2.00±0.03	20	0.32
		Lorentzian		0.80	1.40	78	0.32
				0.83	1.83± 0.02	22	0.32
	180	relaxation	0 ± 700	0.78	1.36	90	0.32
				0.82 ± 0.04	1.66 ± 0.05	10	0.32
		Lorentzian		0.78	1.36	90	0.32
				0.82 ±0.02	1.66 ±0.06	10	0.32
3	80	relaxation	0 ± 40	0.78	1.43	67	0.32
				0.78	2.43	33	0.32
		Lorentzian		0.78	1.43	67	0.32 (49:51)
				0.78	2.43	33	0.32 (54:46)
	110	relaxation	0 ± 40	0.77	1.43	68	0.32
				0.77	2.30	32	0.32
		Lorentzian		0.77	1.43	68	0.32 (51:49)
				0.77	2.30	32	0.32 (54:46)
	150	relaxation	0 ± 70	0.75	1.43	70	0.32
				0.76	2.06	30	0.32
		Lorentzian		0.75	1.43	70	0.32 (51:49)
				0.76	2.06	30	0.32 (54:46)
	200	relaxation	0 ± 90	0.73	1.42	72	0.32
				0.74	1.81	28	0.32
		Lorentzian		0.73	1.42	72	0.32
				0.74	1.81	28	0.32
	250	relaxation	0 ± 350	0.70	1.42	74	0.32
				0.72±0.01	1.66±0.01	26	0.32
		Lorentzian		0.70	1.44	100	0.32 (51:49)

Figure S11. Zero-field ^{57}Fe Mössbauer spectrum of **1** obtained at 105 K. Simulation as an asymmetric Lorentzian doublet with independent areas and linewidths yields the following parameters: δ = 0.79 mm/s, ΔE_Q = 1.25 mm/s, Γ (left) = 0.52 mm/s (47%) and Γ (right) = 0.43 mm/s (53%).

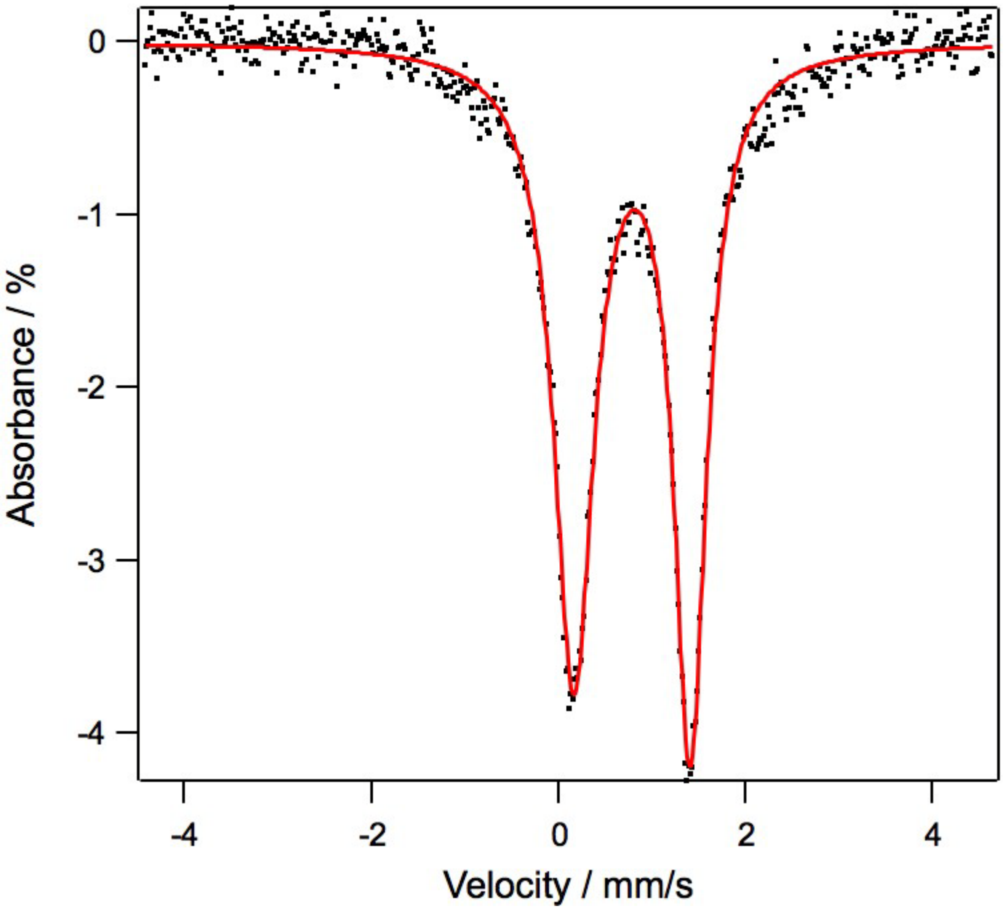

Figure S12. Zero-field ^{57}Fe Mössbauer spectrum of **2** obtained at 4 K, showing Lorentzian fit components (blue and green) and relaxation fit (red). Simulation with Γ held at 0.32 mm/s yields the following parameters: (Lorentzian) δ = 0.83 mm/s, ΔE_Q = 1.57 mm/s (64%, blue trace) and δ = 0.87 mm/s, ΔE_Q = 2.76 mm/s (36%, green trace); (relaxation, red trace) λ = 35 ± 40 kHz, δ = 0.83 mm/s, ΔE_Q = 1.57 mm/s (64%) and δ = 0.87 mm/s, ΔE_Q = 2.76 mm/s (36%).

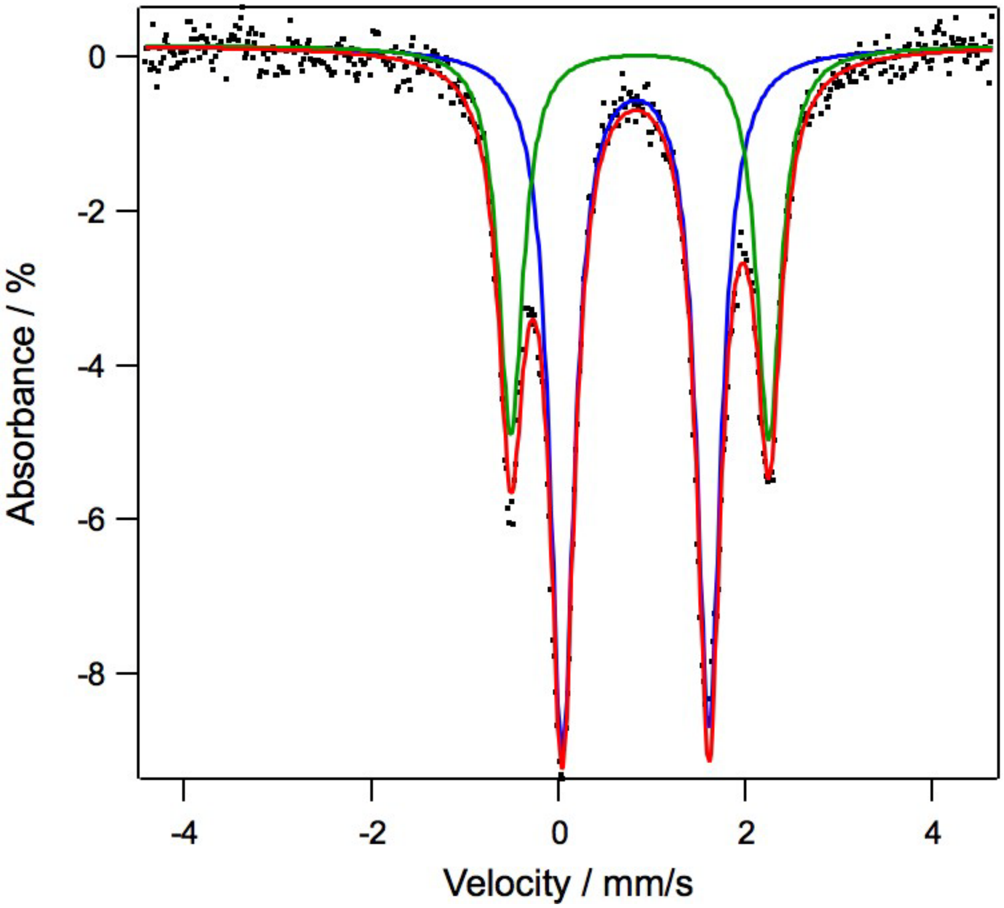

Figure S13. Zero-field ^{57}Fe Mössbauer spectrum of **2** obtained at 50 K, showing Lorentzian fit components (blue and green) and relaxation fit (red). Simulation with Γ held at 0.32 mm/s yields the following parameters: (Lorentzian) $\delta = 0.83$ mm/s, $\Delta E_Q = 1.59$ mm/s (65%, blue trace) and $\delta = 0.88$ mm/s, $\Delta E_Q = 2.71$ mm/s (35%, green trace); (relaxation, red trace) $\lambda = 750 \pm 60$ kHz, $\delta = 0.83$ mm/s, $\Delta E_Q = 1.55$ mm/s (64%) and $\delta = 0.88$ mm/s, $\Delta E_Q = 2.76$ mm/s (36%).

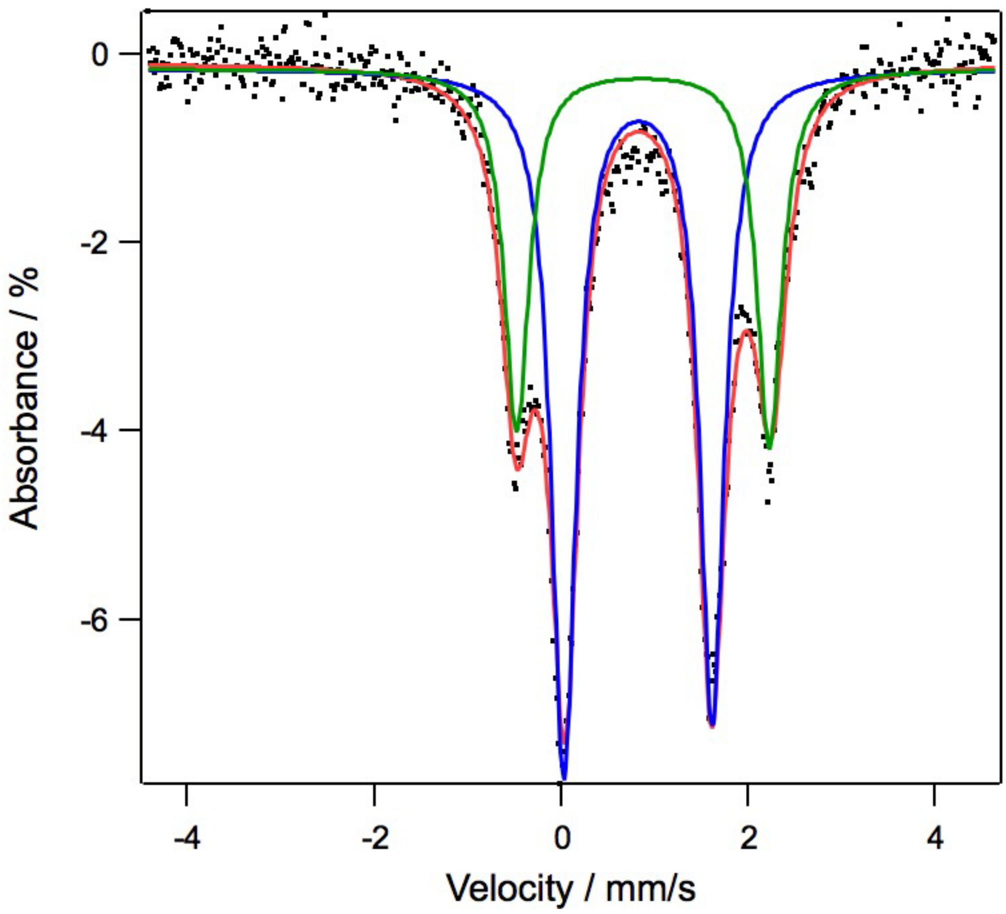

Figure S14. Zero-field ^{57}Fe Mössbauer spectrum of **2** obtained at 105 K, showing Lorentzian fit components (blue and green) and relaxation fit (red). Simulation with Γ held at 0.32 mm/s yields the following parameters: (Lorentzian) δ = 0.82 mm/s, ΔE_Q = 1.48 mm/s (71%, blue trace) and δ = 0.85 mm/s, ΔE_Q = 2.22 mm/s (29%, green trace); (relaxation, red trace) λ = 1110 ± 50 kHz, δ = 0.82 mm/s, ΔE_Q = 1.45 mm/s (70%) and δ = 0.87 mm/s, ΔE_Q = 2.33 mm/s (30%).

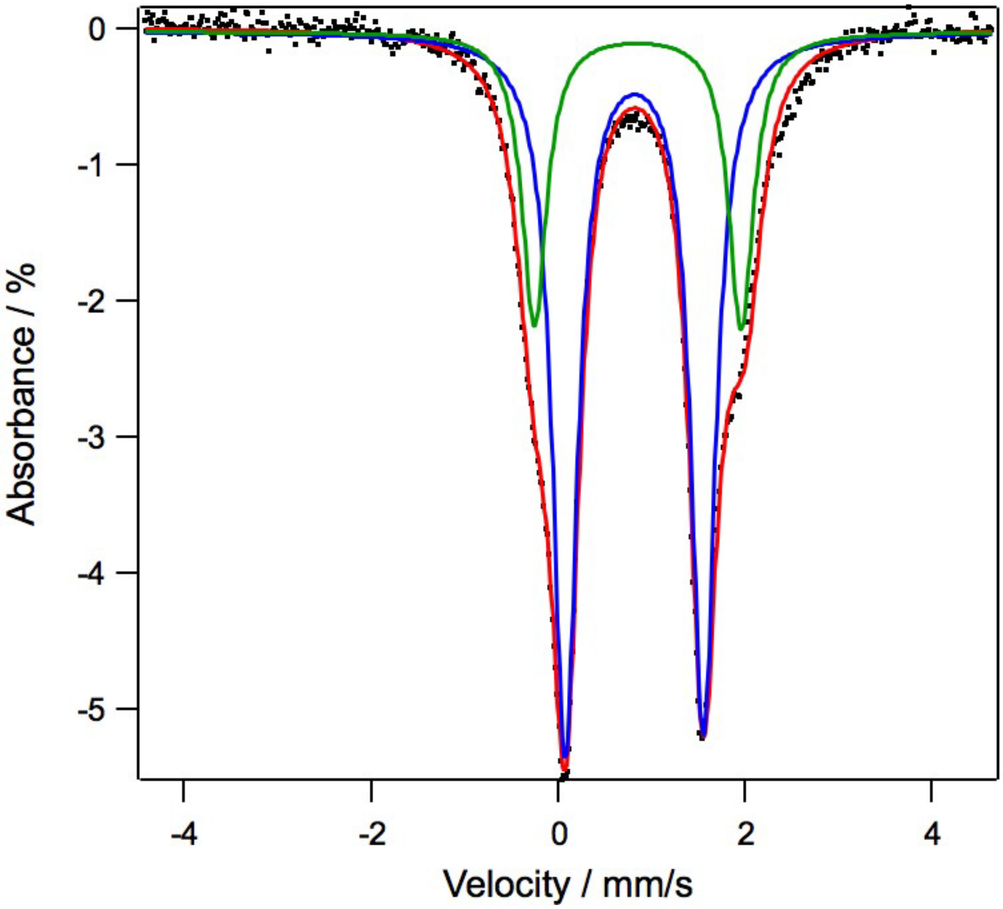

Figure S15. Zero-field ^{57}Fe Mössbauer spectrum of **2** obtained at 150 K, showing Lorentzian fit components (blue and green) and relaxation fit (red). Simulation with Γ held at 0.32 mm/s yields the following parameters: (Lorentzian) δ = 0.80 mm/s, ΔE_Q = 1.40 mm/s (78%, blue trace) and δ = 0.83 mm/s, ΔE_Q = 1.83 mm/s (22%, green trace); (relaxation, red trace) λ = 1290 ± 350 kHz, δ = 0.80 mm/s, ΔE_Q = 1.37 mm/s (80%) and δ = 0.85 ± 0.02 mm/s, ΔE_Q = 2.00 ± 0.03 mm/s (20%).

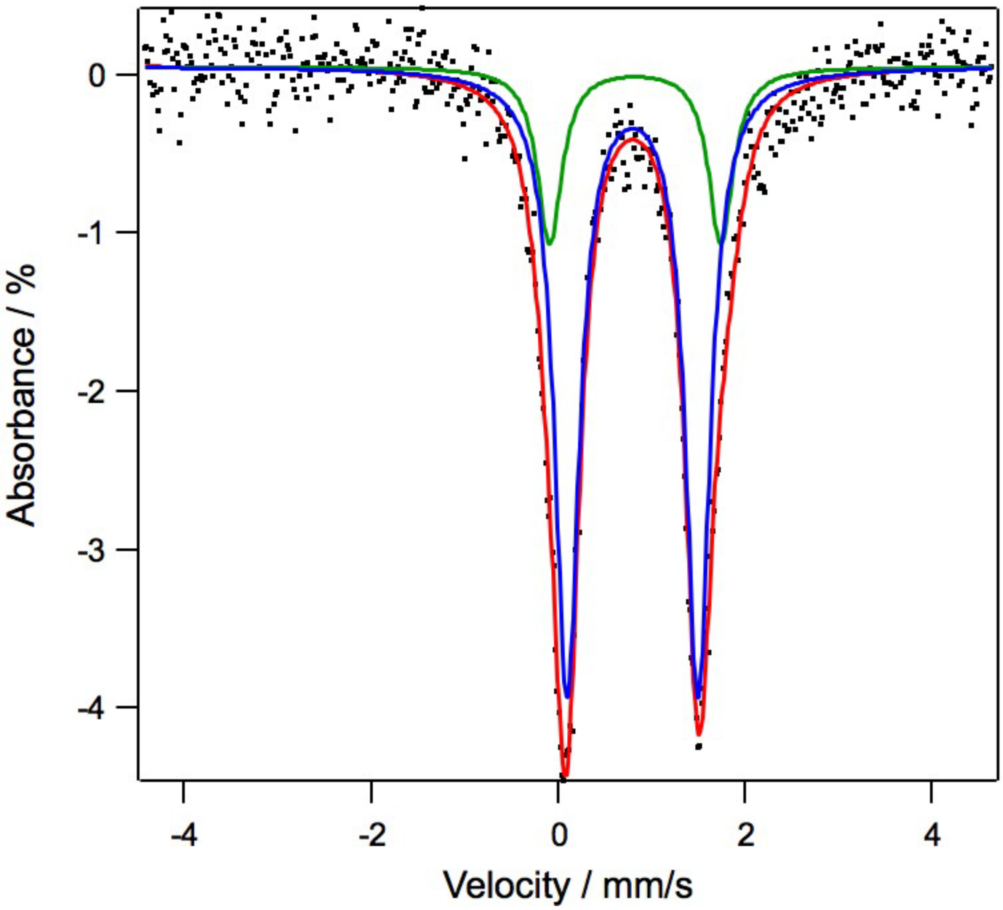

Figure S16. Zero-field ^{57}Fe Mössbauer spectrum of **2** obtained at 180 K, showing Lorentzian fit components (blue and green) and relaxation fit (red). Simulation with Γ held at 0.32 mm/s yields the following parameters: (Lorentzian) $\delta = 0.78$ mm/s, $\Delta E_Q = 1.36$ mm/s (90%, blue trace) and $\delta = 0.82 \pm 0.02$ mm/s, $\Delta E_Q = 1.66 \pm 0.06$ mm/s (10%, green trace); (relaxation, red trace) $\lambda = 0 \pm 700$ kHz, $\delta = 0.78$ mm/s, $\Delta E_Q = 1.36$ mm/s (90%) and $\delta = 0.82 \pm 0.04$ mm/s, $\Delta E_Q = 1.66 \pm 0.05$ mm/s (10%).

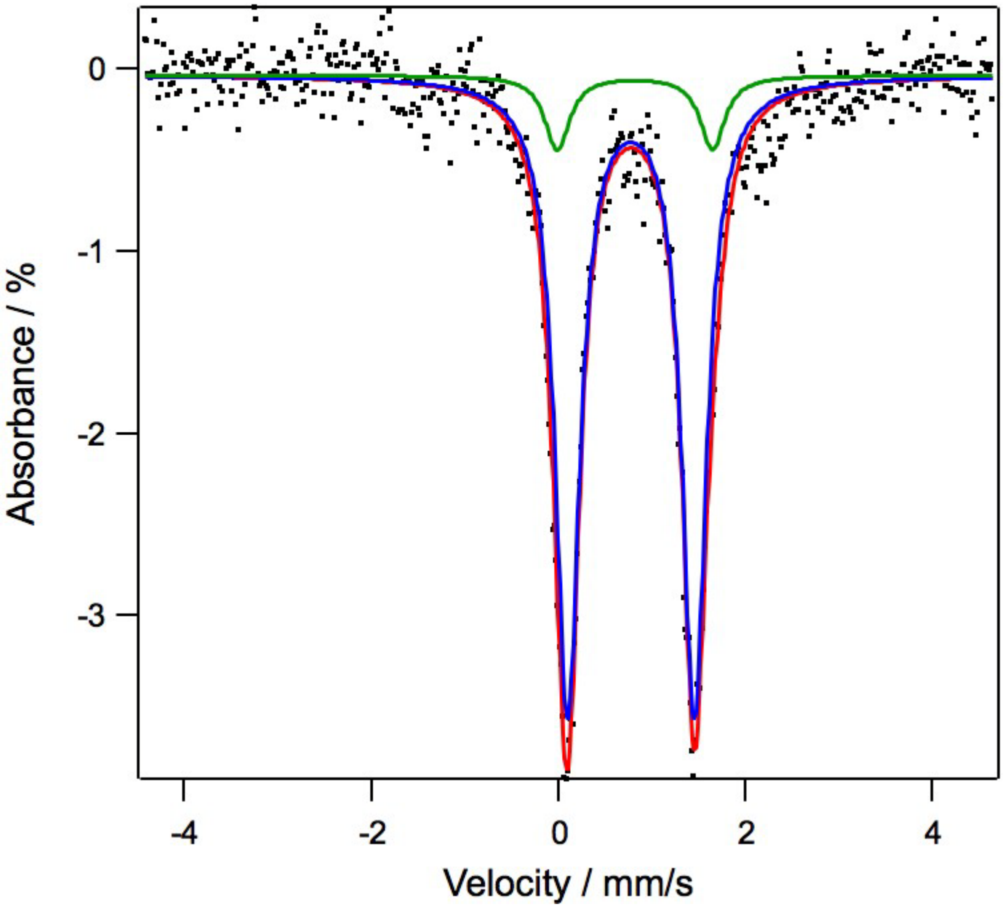

Figure S17. Zero-field ^{57}Fe Mössbauer spectrum of **3** obtained at 80 K, showing Lorentzian fit components (blue and green) and relaxation fit (red). Simulation with Γ held at 0.32 mm/s yields the following parameters: (Lorentzian) δ = 0.78 mm/s, ΔE_Q = 1.43 mm/s (67%, blue trace) and δ = 0.78 mm/s, ΔE_Q = 2.43 mm/s (33%, green trace); (relaxation, red trace) λ = 0 ± 40 kHz, δ = 0.78 mm/s, ΔE_Q = 1.43 mm/s (67%) and δ = 0.78 mm/s, ΔE_Q = 2.43 mm/s (33%).

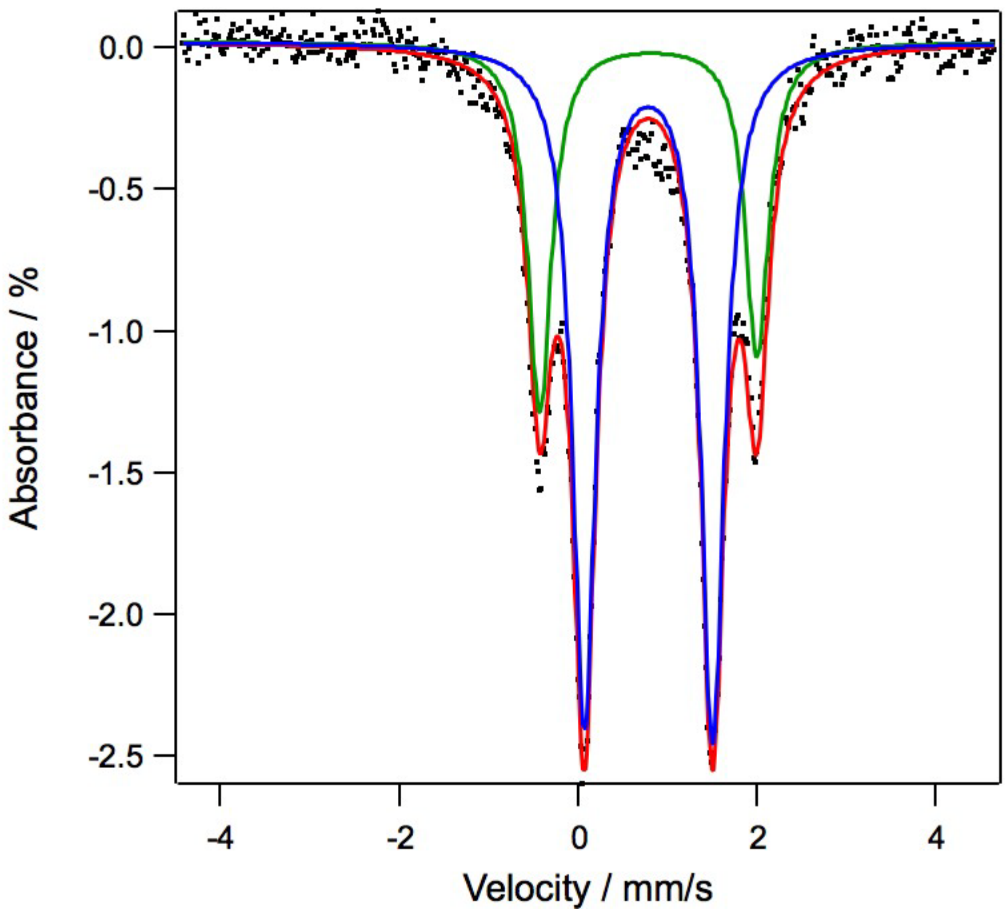

Figure S18. Zero-field ^{57}Fe Mössbauer spectrum of **3** obtained at 110 K, showing Lorentzian fit components (blue and green) and relaxation fit (red). Simulation with Γ held at 0.32 mm/s yields the following parameters: (Lorentzian) $\delta = 0.77$ mm/s, $\Delta E_Q = 1.43$ mm/s (68%, blue trace) and $\delta = 0.77$ mm/s, $\Delta E_Q = 2.30$ mm/s (32%, green trace); (relaxation, red trace) $\lambda = 0 \pm 40$ kHz, $\delta = 0.77$ mm/s, $\Delta E_Q = 1.43$ mm/s (68%) and $\delta = 0.77$ mm/s, $\Delta E_Q = 2.30$ mm/s (32%).

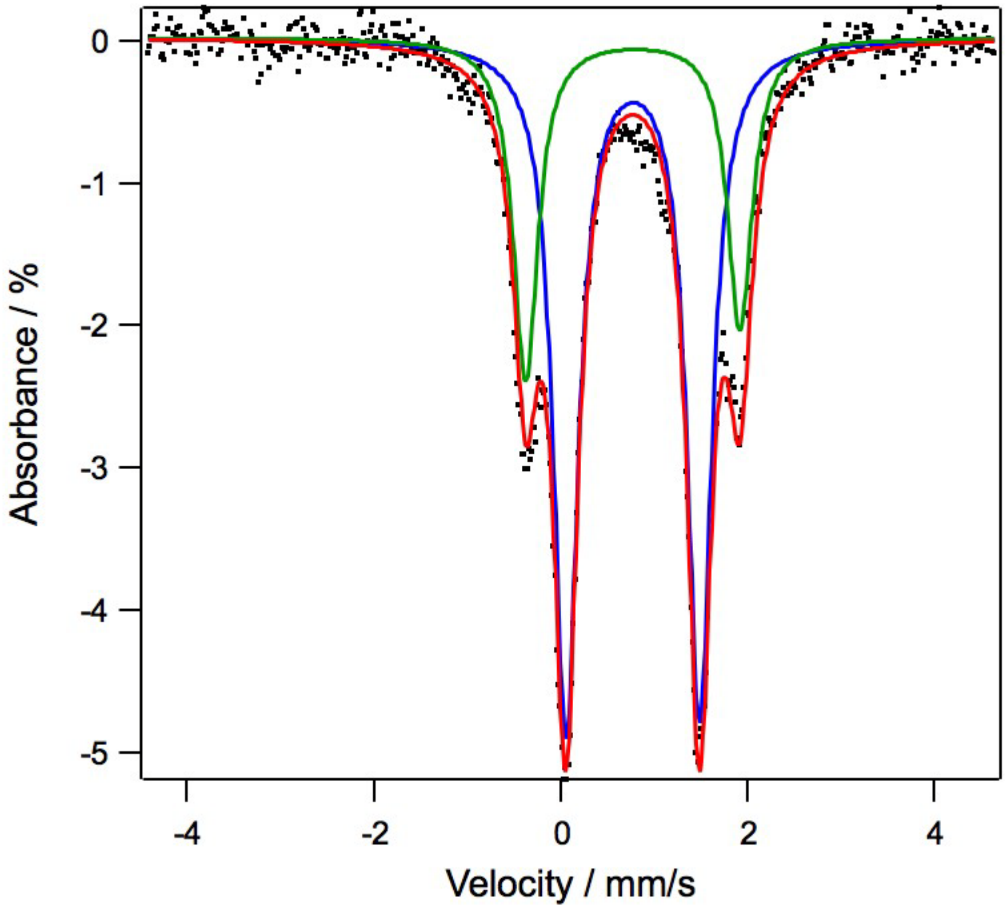

Figure S19. Zero-field ^{57}Fe Mössbauer spectrum of **3** obtained at 150 K, showing Lorentzian fit components (blue and green) and relaxation fit (red). Simulation with Γ held at 0.32 mm/s yields the following parameters: (Lorentzian) δ = 0.75 mm/s, ΔE_Q = 1.43 mm/s (70%, blue trace) and δ = 0.76 mm/s, ΔE_Q = 2.06 mm/s (30%, green trace); (relaxation, red trace) $\lambda = 0 \pm 70$ kHz, δ = 0.75 mm/s, ΔE_Q = 1.43 mm/s (70%) and δ = 0.76 mm/s, ΔE_Q = 2.06 mm/s (30%).

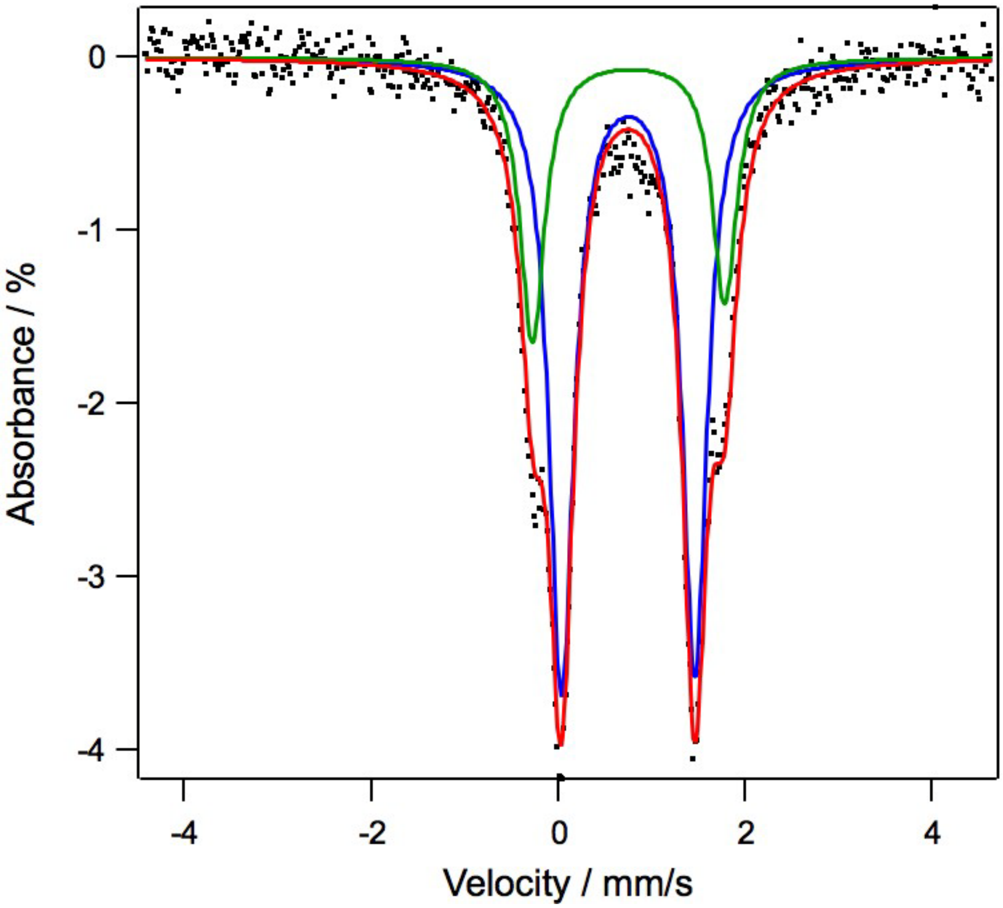

Figure S20. Zero-field ^{57}Fe Mössbauer spectrum of **3** obtained at 200 K, showing Lorentzian fit components (blue and green) and relaxation fit (red). Simulation with Γ held at 0.32 mm/s yields the following parameters: (Lorentzian) δ = 0.73 mm/s, ΔE_Q = 1.42 mm/s (72%, blue trace) and δ = 0.74 mm/s, ΔE_Q = 1.81 mm/s (28%, green trace); (relaxation, red trace) $\lambda = 0 \pm 90$ kHz, δ = 0.73 mm/s, ΔE_Q = 1.42 mm/s (72%) and δ = 0.74 mm/s, ΔE_Q = 1.81 mm/s (28%).

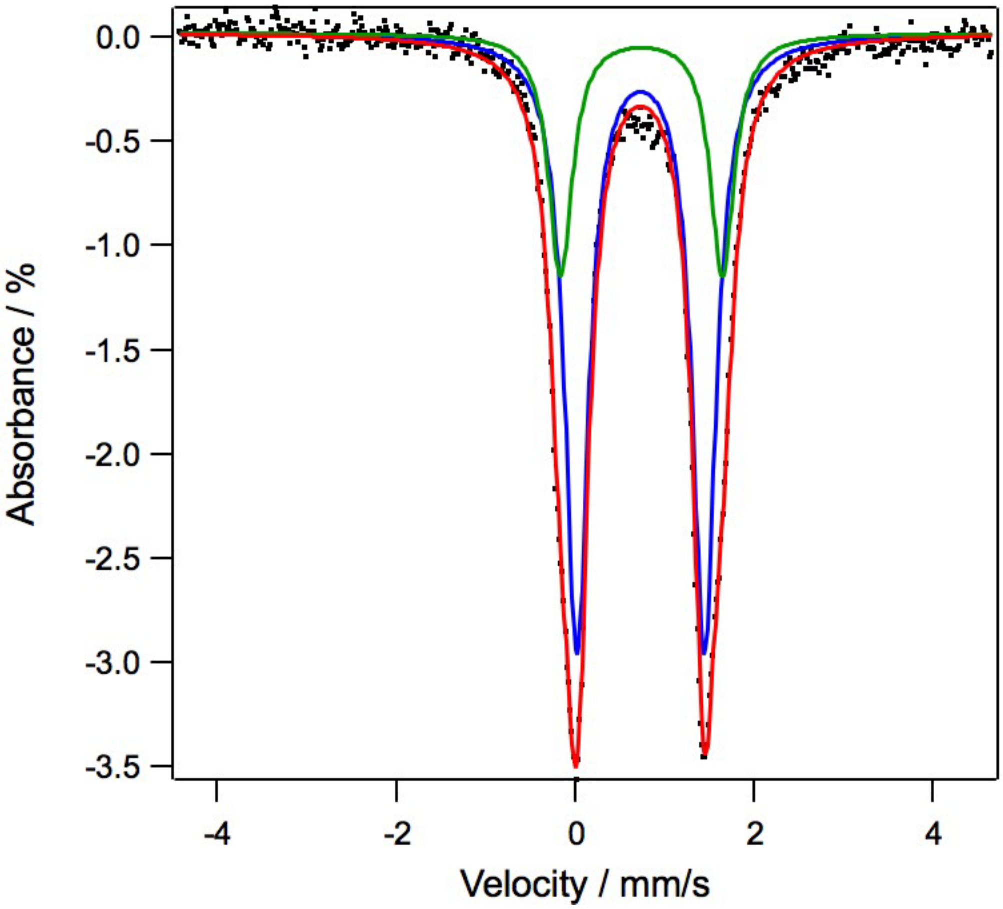

Figure S21. Zero-field ^{57}Fe Mössbauer spectrum of **3** obtained at 250 K, showing Lorentzian fit components (blue and green) and relaxation fit (red). Simulation with Γ held at 0.32 mm/s yields the following parameters: (Lorentzian) δ = 0.70 mm/s, ΔE_Q = 1.44 mm/s (left 51%, right 49%, blue trace); (relaxation, red trace) λ = 0 ± 350 kHz, δ = 0.70 mm/s, ΔE_Q = 1.42 mm/s (74%) and δ = 0.72 ± 0.01 mm/s, ΔE_Q = 1.66 ± 0.01 mm/s (26%).

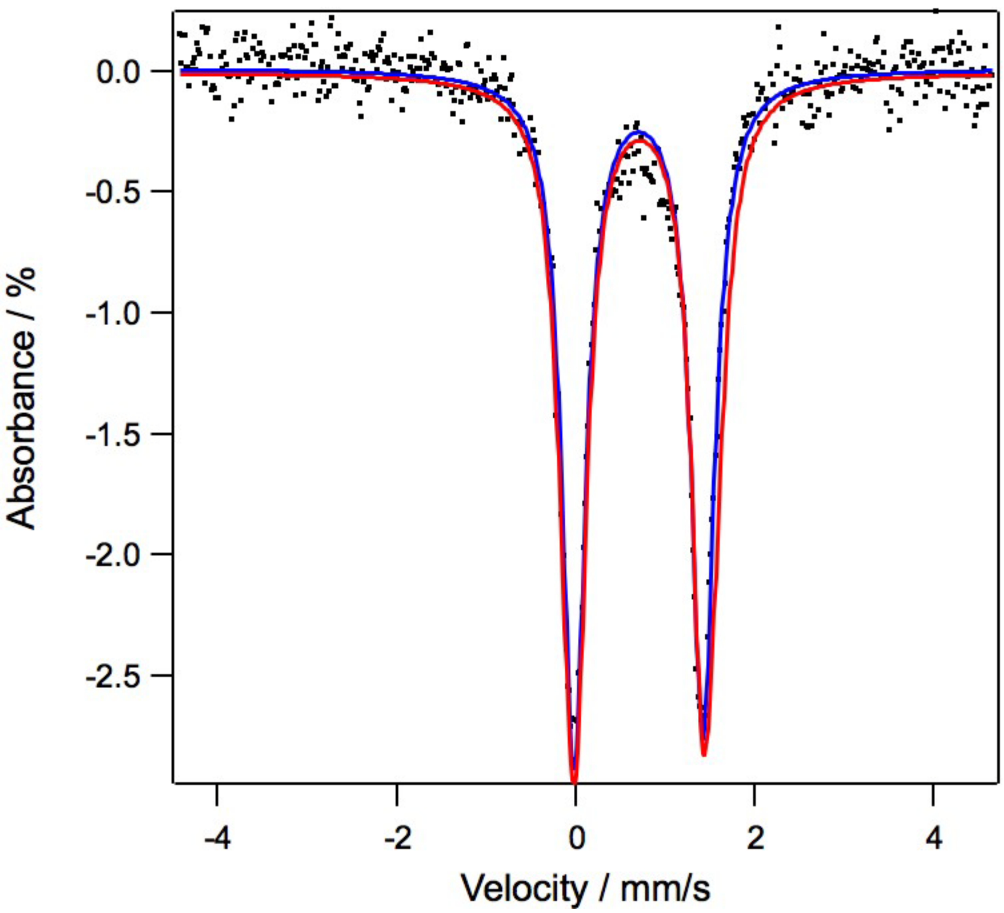

Figure S22. Variable-temperature magnetic susceptibility data for **1** collected under various fields.

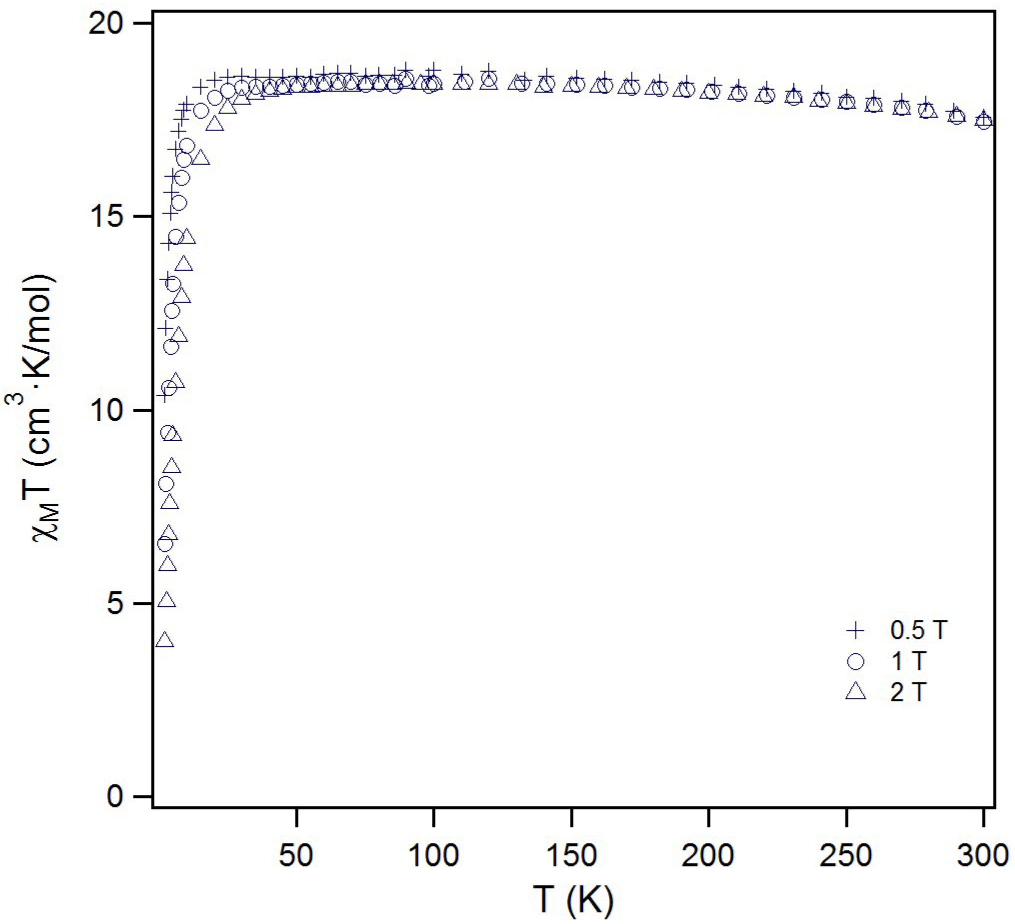

Figure S23. Curie-Weiss plot for **1** at various fields.

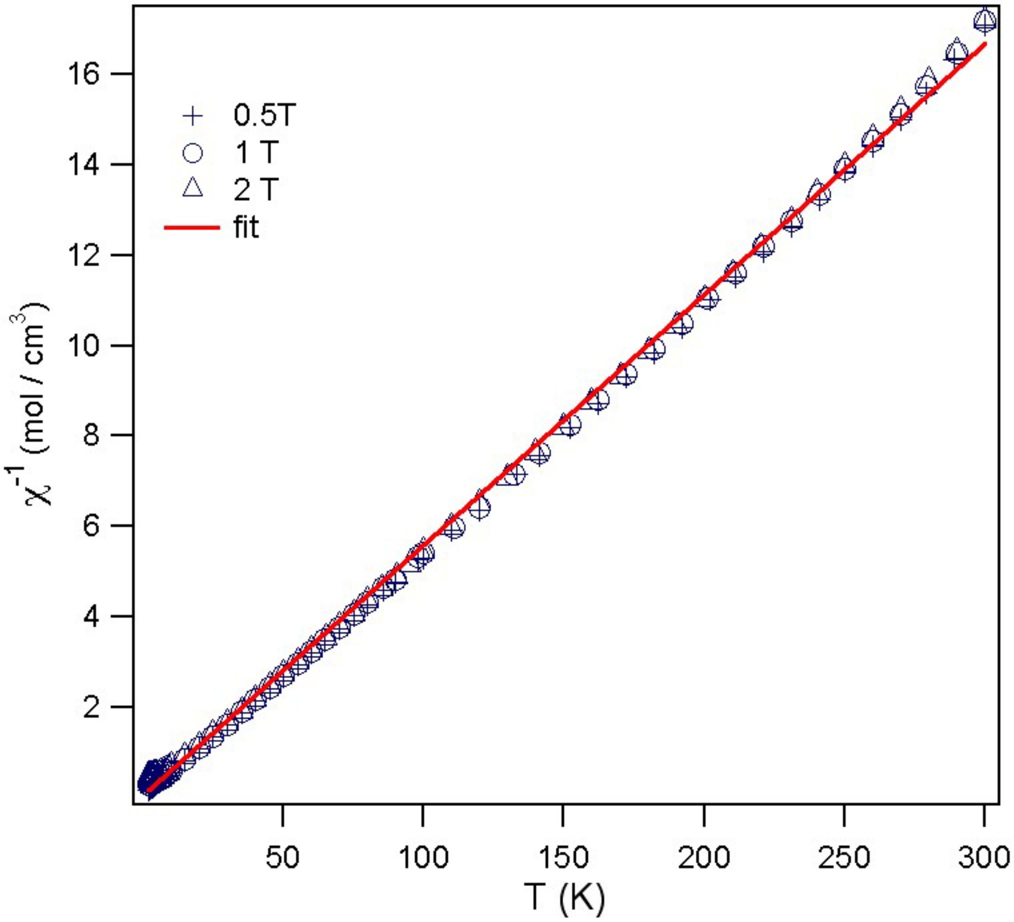

Figure S24. Variable-temperature magnetization data for **1** collected at various fields. Solid black lines correspond to fits to the data, as described in the text ($D = +1.7$ cm^{-1}, $|E| = 0.3$ cm^{-1}, and $g = 2.3$), for $S = 5$.

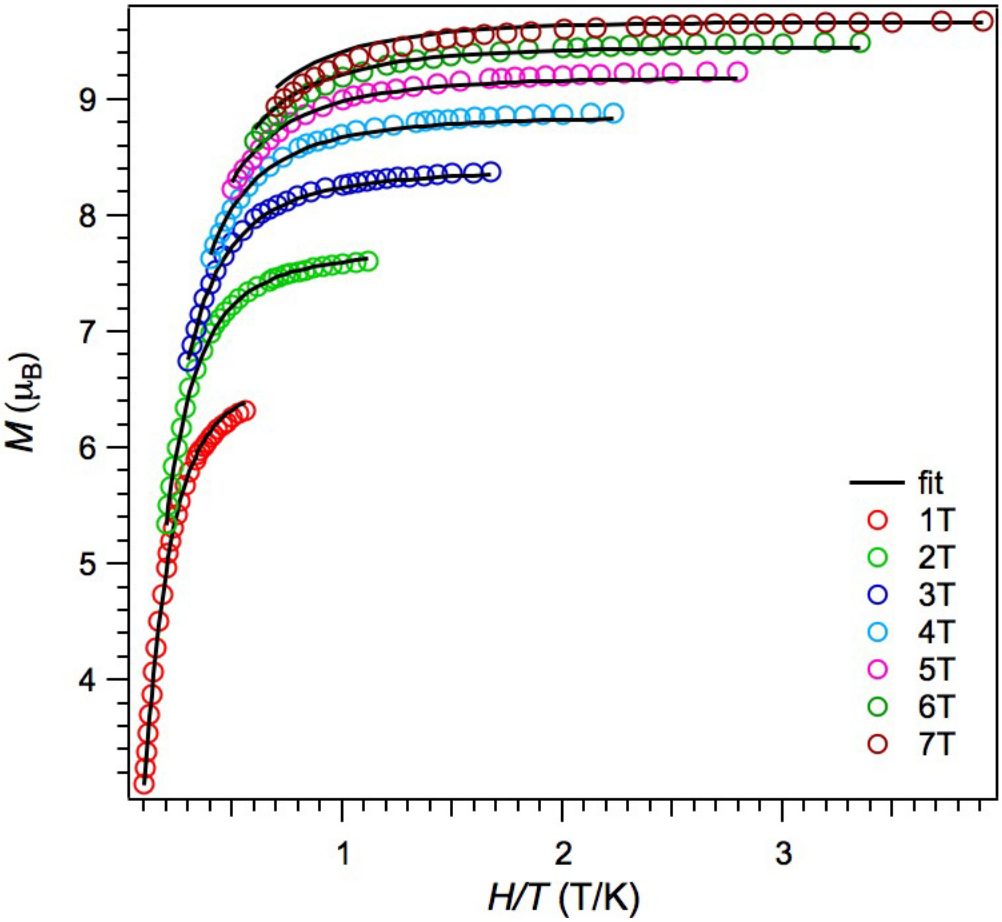

Figure S25. Variable-temperature magnetic susceptibility data for **2** collected under various fields.

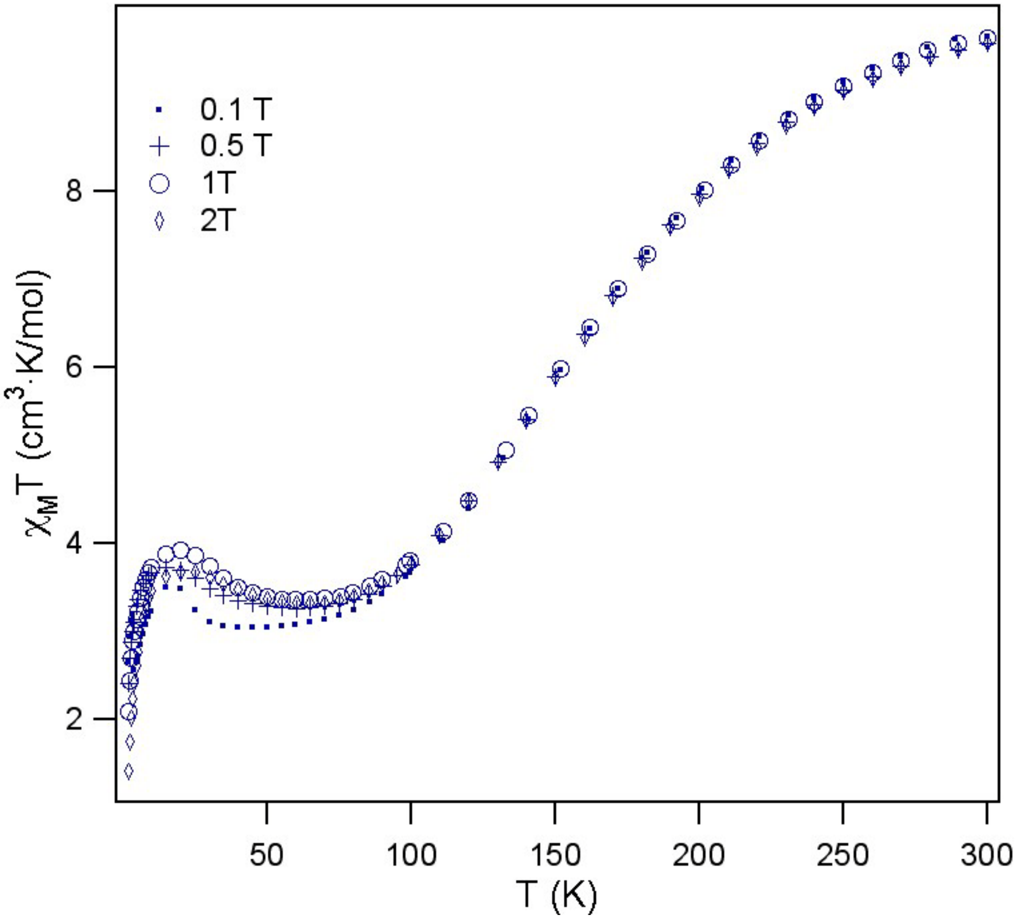

Figure S26. Curie-Weiss plot for **2** at various fields.

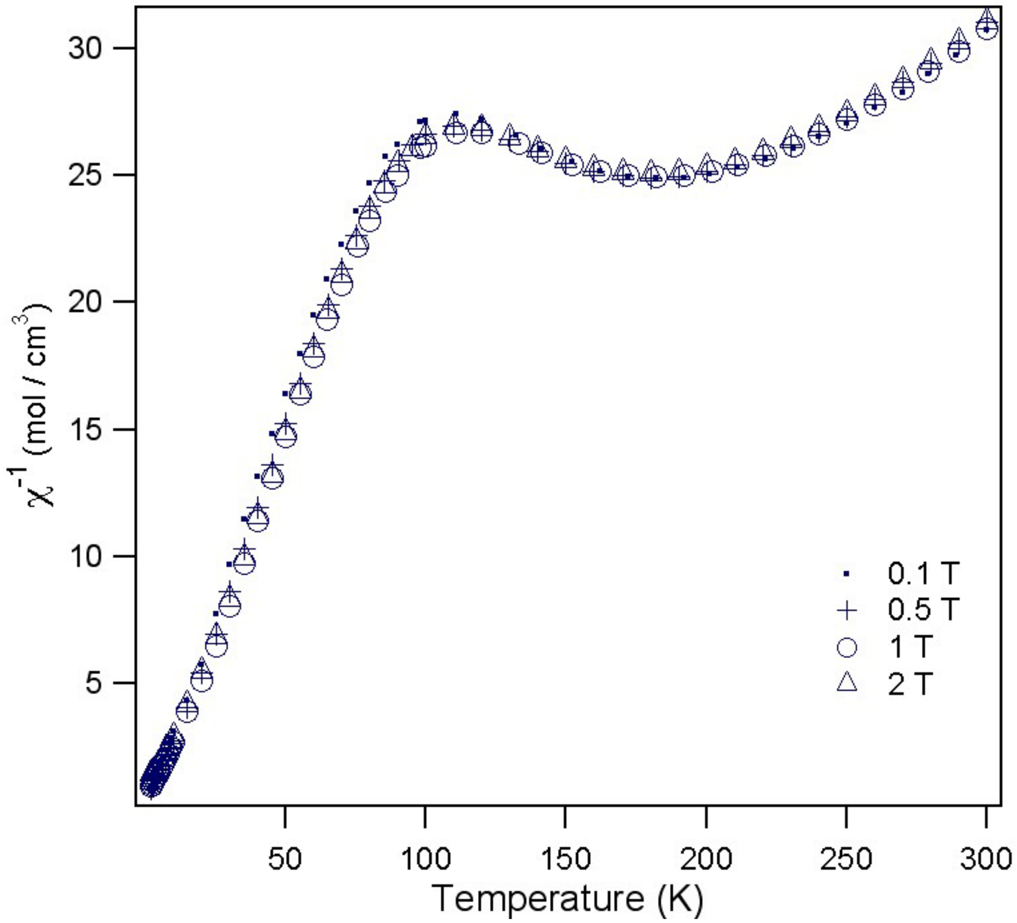

Figure S27. Variable-temperature magnetic susceptibility data for **2** collected under a field of 0.1 T. The solid lines correspond to various simulations, as described in the text, with *J* given in cm^{-1}.

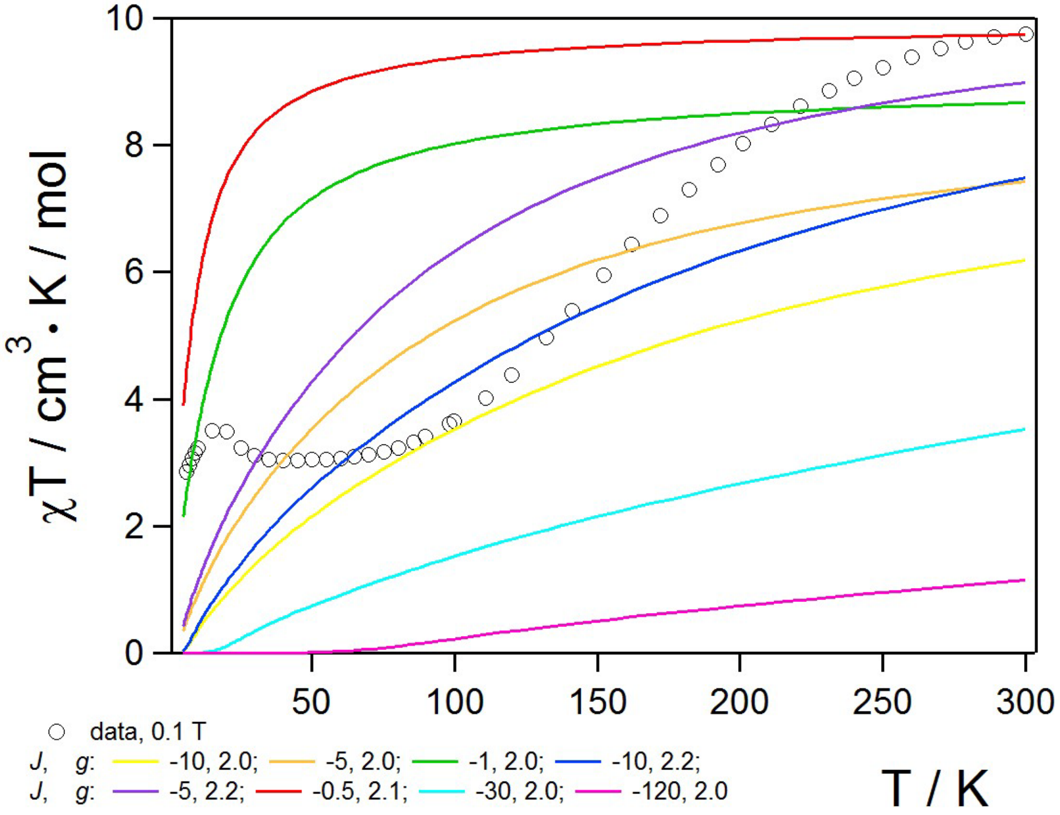

Figure S28. Variable-temperature magnetic susceptibility data for **2** collected under a field of 0.1 T. The solid lines correspond to various simulations, as described in the text, with *J* given in cm^{-1}.

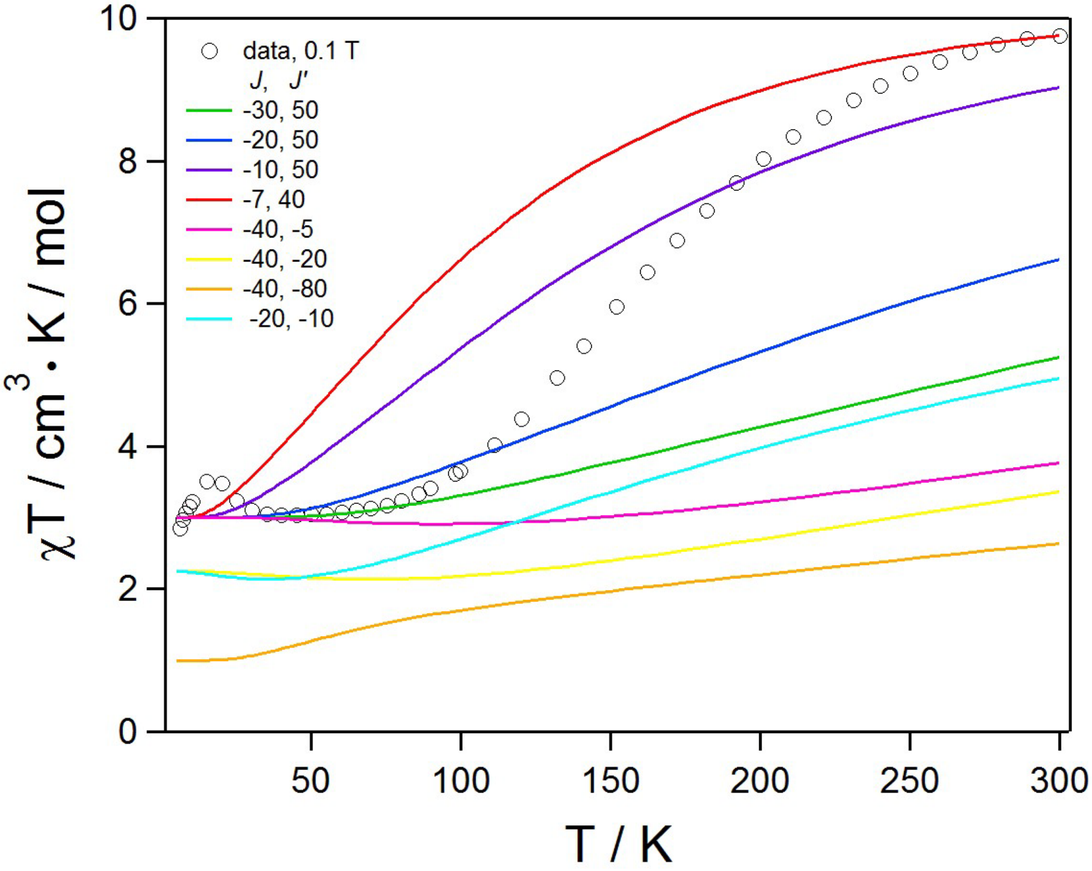

Figure S29. Variable-temperature magnetic susceptibility data for **2** collected under a field of 0.1 T. The solid lines correspond to various simulations, as described in the text, with *J* given in cm^{-1}.

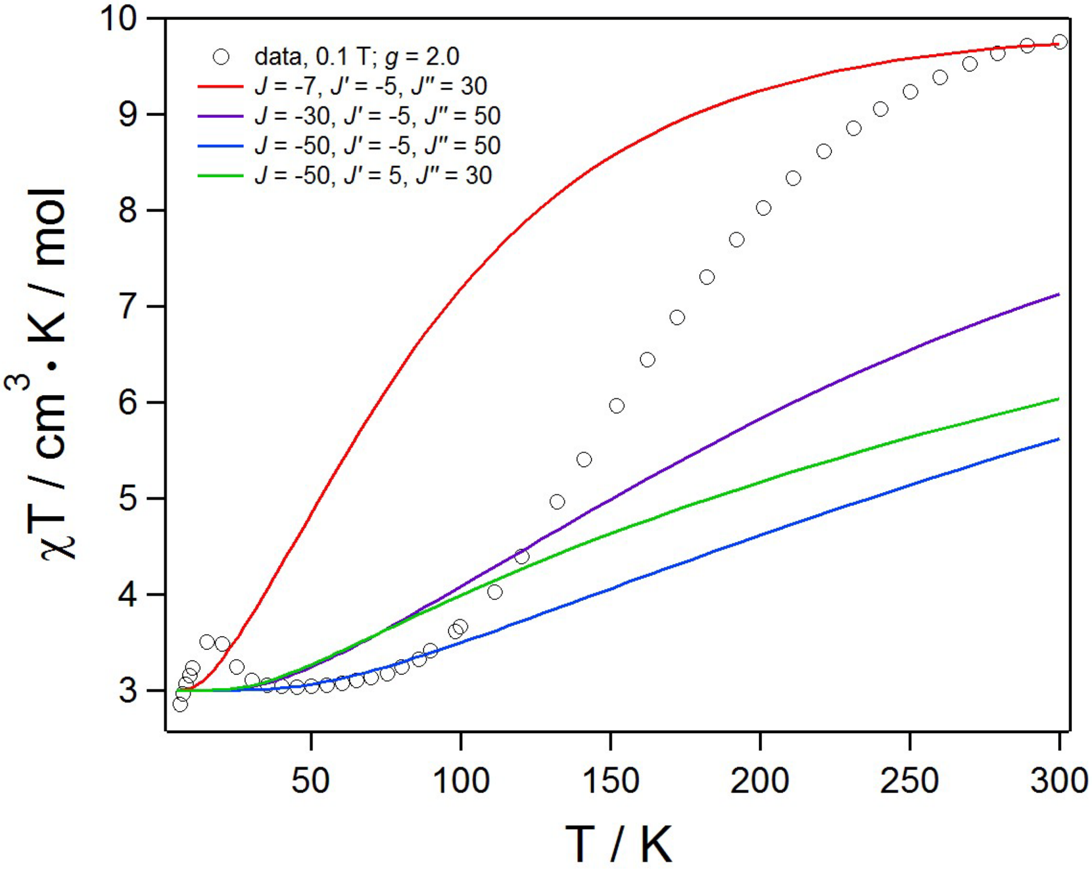

Figure S30. Variable-temperature magnetization data for **2** collected at various fields. The solid black lines correspond to fits to the data, as described in the text.

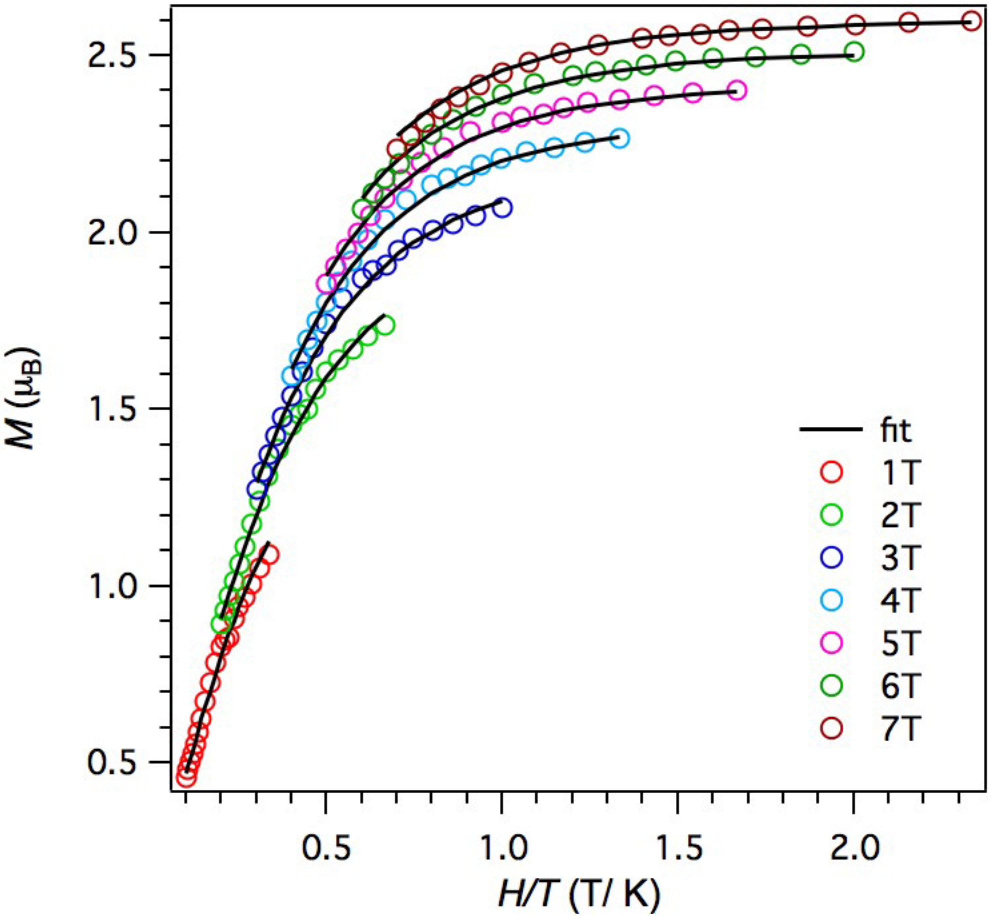

Figure S31. Variable-temperature magnetic susceptibility data for **3** collected under various fields.

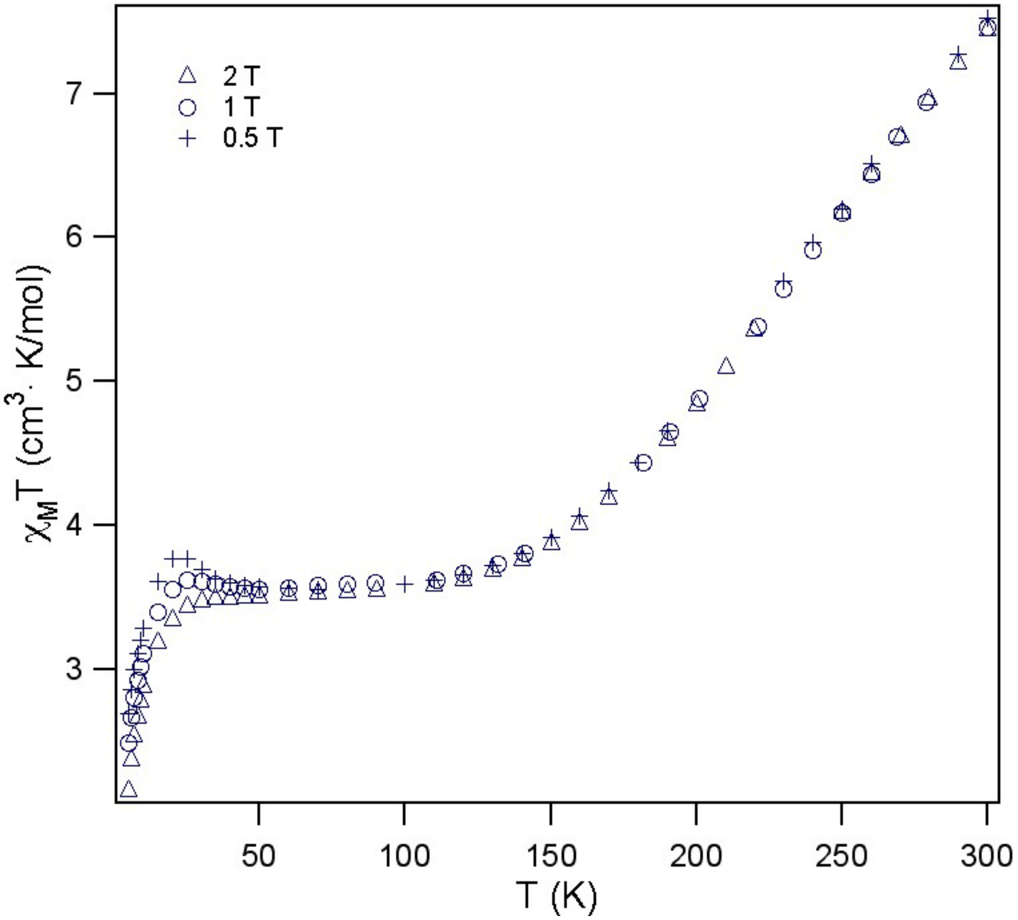

Figure S32. Curie-Weiss plot for **3** at various fields.

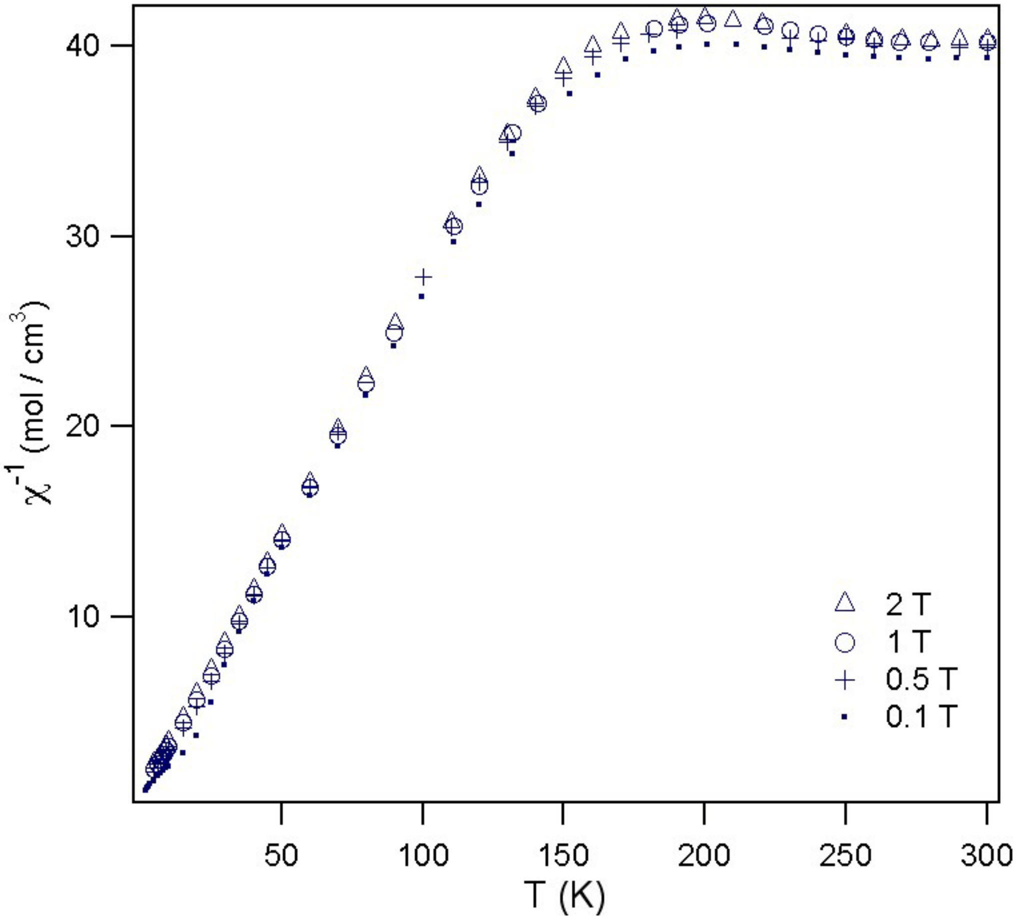

Figure S33. Variable-temperature magnetic susceptibility data for **3** collected under a field of 1 T. The solid lines correspond to various simulations, as described in the text, with *J* given in cm^{-1}.

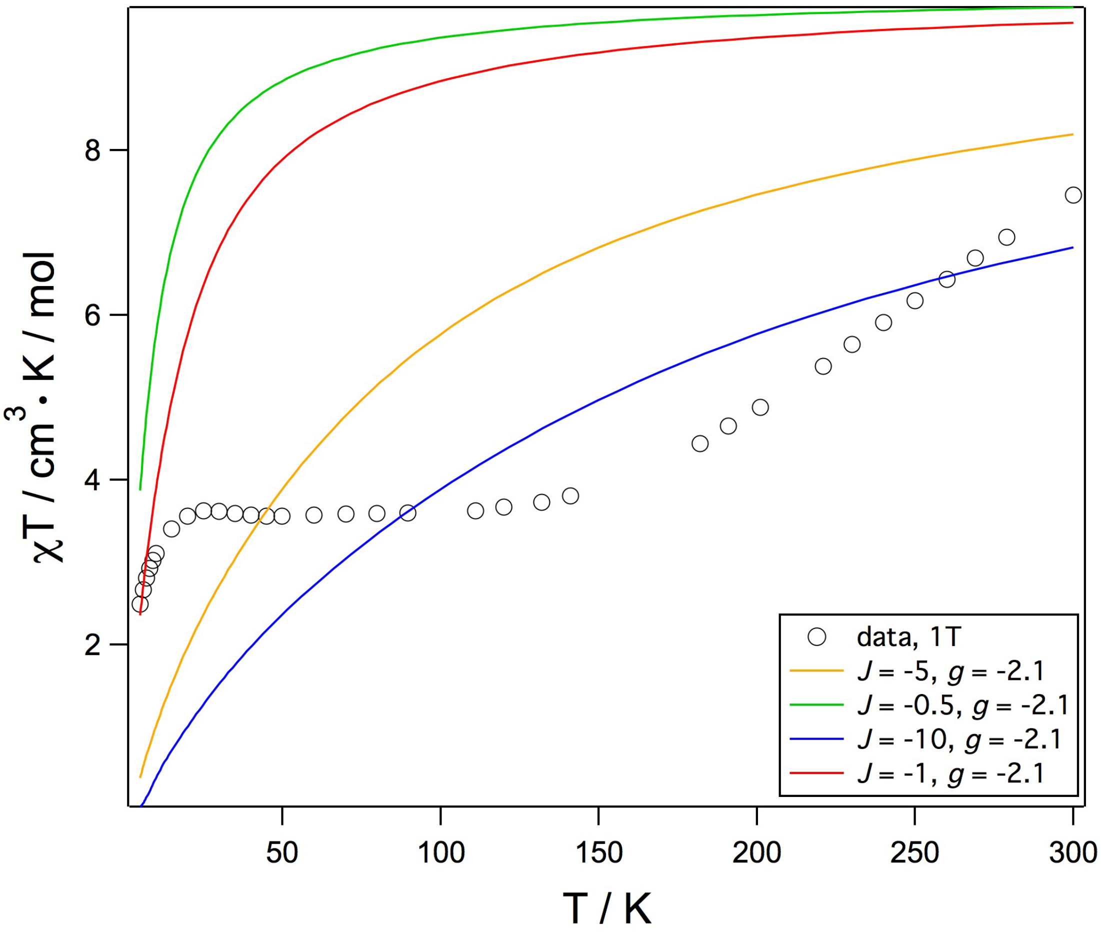

Figure S34. Variable-temperature magnetic susceptibility data for **3** collected under a field of 1 T. The solid lines correspond to various simulations, as described in the text, with *J* given in cm^{-1}.

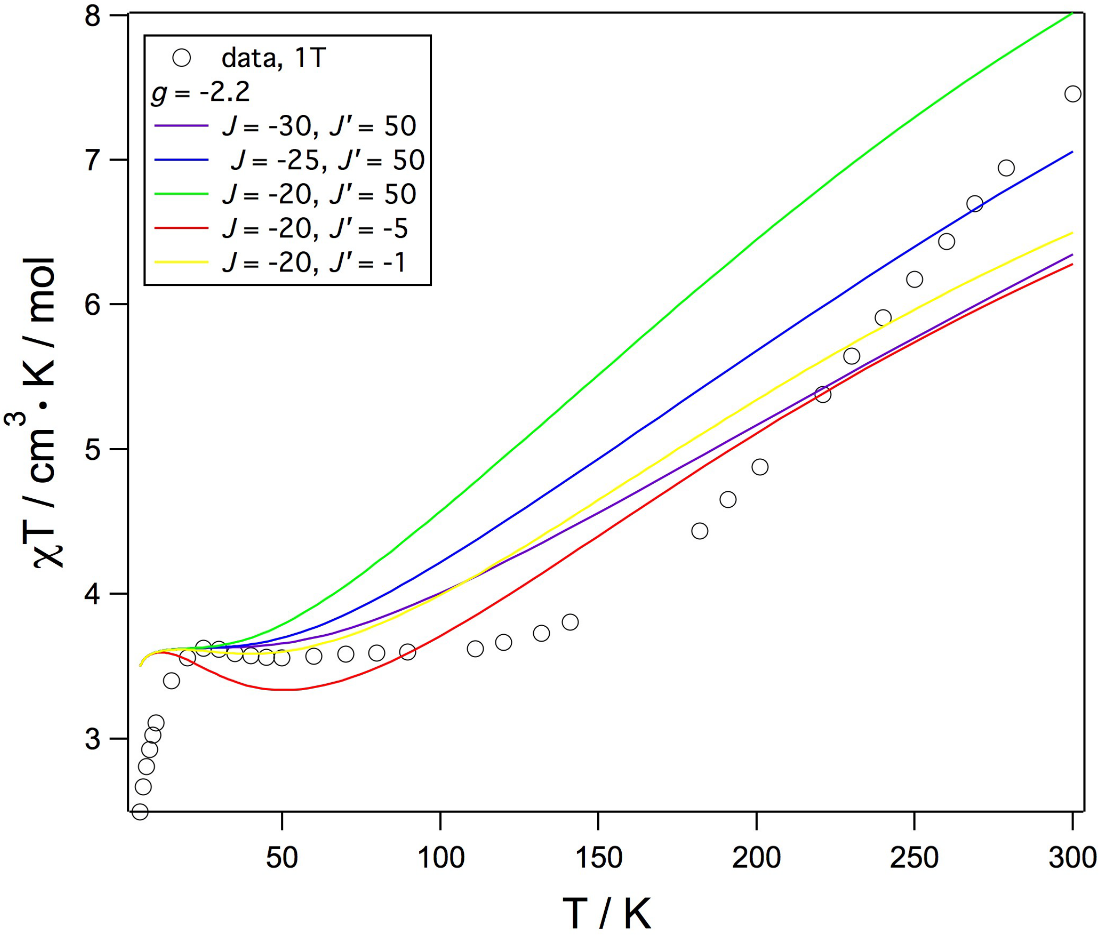

Figure S35. Variable-temperature magnetic susceptibility data for **3** collected under a field of 1 T. The solid lines correspond to various simulations, as described in the text, with *J* given in cm^{-1}.

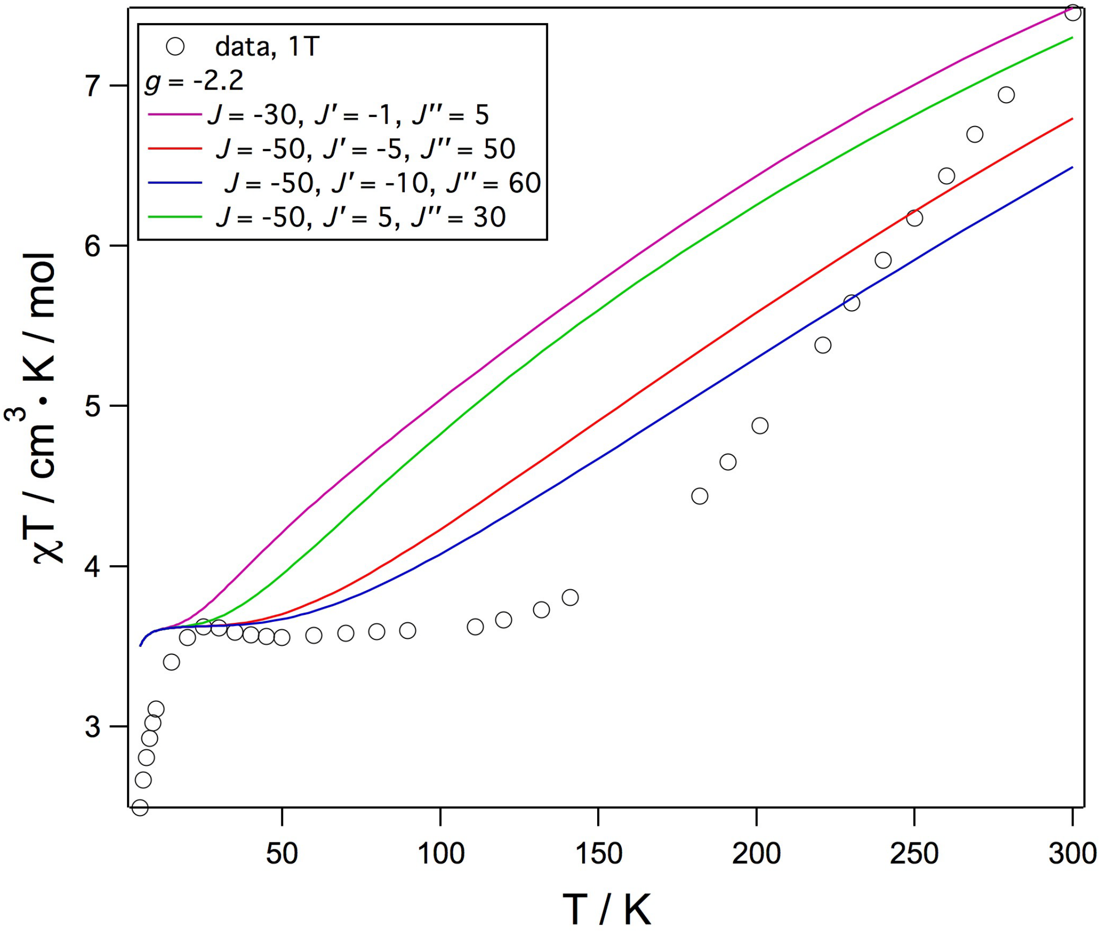

Figure S36. Variable-temperature magnetization data for **3** collected at various fields. The solid black lines correspond to fits to the data, as described in the text.